

PII: S0079-6107(96)00011-9

X-RAY COMPUTED MICROTOMOGRAPHY (μ CT) USING SYNCHROTRON RADIATION (SR)

ULRICH BONSE and FRANK BUSCH

Institute of Physics, University of Dortmund, D-44221 Dortmund, Germany

CONTENTS

I. INTRODUCTION	133
II. PRINCIPLE AND TECHNIQUES OF X-RAY MICROTOMOGRAPHY	135
2.1. <i>Projection and Reconstruction</i>	135
2.2. <i>Projection Modes</i>	139
2.2.1. <i>Parallel beam geometry</i>	139
2.2.1.1. <i>Point scanning</i>	139
2.2.1.2. <i>Line scanning</i>	140
2.2.1.3. <i>Parallel projection</i>	140
2.2.2. <i>Conebeam geometry</i>	140
2.2.2.1. <i>Fan scanning</i>	140
2.2.2.2. <i>Cone projection</i>	140
2.3. <i>X-ray Sources and Detectors</i>	141
2.3.1. <i>X-ray sources</i>	141
2.3.2. <i>X-ray detectors</i>	144
2.4. <i>Contrast Mechanisms</i>	148
2.4.1. <i>Absorption contrast</i>	148
2.4.2. <i>Differential absorption contrast</i>	150
2.5. <i>Resolution and Statistical Accuracy</i>	151
III. RESULTS	153
3.1. <i>Point Scanning</i>	153
3.2. <i>Line Scanning</i>	154
3.3. <i>Cone Projection and Fan Scanning</i>	155
3.4. <i>Parallel Projection</i>	156
3.5. <i>Phase-contrast μCT</i>	161
IV. OUTLOOK	164
ACKNOWLEDGEMENTS	165
REFERENCES	165

I. INTRODUCTION

Imaging methods have always played a major role as research tools in medicine and biology. With increasing tendency to study more directly the underlying building blocks of life objects, i.e. cells and macromolecules and their basic arrays, the capacity of imaging techniques to reveal structural details on a smaller scale gained importance. Therefore light microscopy which has a spatial resolution limit of about $0.5 \mu\text{m}$ was complemented by electron microscopy which, under most favourable conditions, is capable of resolving single atoms less than 1 nm in size. X-Ray microscopy has extended its resolution limit down to 30 nm (Meyer-Ilse *et al.*, 1992) and is becoming a valuable research tool in medicine and biology. On the other hand, X-ray holography (McNulty *et al.*, 1992a,b; McNulty 1994; Chen *et al.*, 1995) has been developing steadily and considerable progress with regard to resolution and image quality has been achieved over the last decade. The best holographic three-dimensional (3D) resolution reached so far is that of a grid with 50–60 nm lines laterally and about 100 nm resolution in depth. However, images obtained still contain more noise than with any of the other methods.

Besides spatial resolution there are also other, often equally important aspects from which one has to judge the value of a given imaging technique when applying it to medical and biological research.

One is sample preparation which should be least invasive in order not to change the sample's properties too much on preparing it. The ideal case of imaging specimens *in vivo* is with X-rays often feasible, since they penetrate almost all medical and biological samples fairly well. On the other hand, by virtue of using much more powerful lenses for imaging than are available for X-rays, light and electron microscopy are capable of directly producing pictures of high quality that contain ample structural information. For the light microscope, sample opaqueness and/or scattering by artefacts can cause difficulties. Electron-microscopic imaging normally requires the sample to be dried, contrasted and transferred into vacuum. Structural changes suffered by the sample undergoing preparation for electron-microscopic imaging can be severe.

Furthermore, the optimum structural information is obtained if imaging in 3D is possible. The normal way to achieve this is to section the sample, making two-dimensional (2D) images of all sections, and then compose them by a special rendering algorithm to yield the required 3D information. Since electron- and light-microscopic images are usually generic 2D images this is the most commonly followed procedure in these cases. Its inherent disadvantage is the need to destroy the original sample by histologic sectioning, which, for instance, makes it impossible to obtain additional structure information by looking a second time at the same sample.

In the case of light microscopy, however, confocal optical microscopy as developed by Boyde and co-workers (Petran *et al.*, 1985; Boyde, 1985; Boyde *et al.*, 1990) can be considered an exception to this rule. With this technique, light originating at object points lying outside the focal plane of the objective is excluded from contributing to the microscopic image with the help of special optical means. The focal plane thus defines a "section" through the sample without the need to cut it into slices. By stepwise positioning of the focal plane at different depths below the surface, 3D information of the sample is collected. Obviously the application of this method is restricted to translucent samples of a size not exceeding the working distance of microscope objectives that yield sufficient magnification.

In the X-ray case the situation regarding 3D imaging is mixed. In its present state, X-ray holography does not yet yield usable 3D pictures (McNulty *et al.*, 1992a). X-Ray microscopy yields 2D images from the beginning, however the art of making 3D images by this method has only just begun (Lehr, 1996). On the other hand, as was already pointed out, X-rays penetrate all light materials fairly well and projection images taken with X-rays, although having a 2D format, essentially carry partial 3D information of the total sample volume traversed in the projection. As is well known by now, full 3D information is obtainable by taking projection images of the same sample volume in a number of different directions. The projections are then used as input for the computerized tomographic reconstruction of the 3D sample. This technique (Hounsfield, 1973), known as Computerized X-ray Tomography (CT) is widely used in the medical field at spatial resolutions above about 200 μm . The other tomographic imaging tool which is likewise important and also well established in the medical field is NMR-tomography. There, its spatial resolution is of the order of 500–1000 μm . For non-medical applications the measuring time can be greatly increased so that spatial resolutions of the order of 5 μm become possible (Zhou and Lauterbur, 1992).

On X-ray tomograms specimen parts of higher density, like bones etc., give larger contrast than parts of lower density. Quite different from this, medical NMR tomograms show the distribution of hydrogen in organic matter. Of principal interest for the structural investigation of medical and biological specimens is also ion microbeam tomography (Huddleston *et al.*, 1982; Ito and Koyama-Ito, 1984; Pontau *et al.*, 1989; Fischer and Mühlbauer, 1990; Pontau *et al.*, 1990). On traversing the specimen, ions lose part of their kinetic energy. The energy loss increases with specimen density which is then mapped in 3D after reconstruction. The technique is especially useful for samples where

large variations in atomic number Z or low total density limit the applicability of X-ray tomography. Best diagnostic information about the functioning of organs, of tissues and of blood flow may be obtained from tracer emission tomographies like single photon emission computer tomography (SPECT) or positron emission tomography (PET).

It will be the main subject of this article to show that due to the development of high intensity synchrotron sources the spatial resolution of CT using X-rays has been extended down to the order of $1\ \mu\text{m}$ and below. As a consequence of this, new scientific problems can now be tackled with X-ray tomography using synchrotron radiation. For comparison and in order to further illustrate the technical development achieved, we include some early key experiments using microbeams in which conventional X-ray tubes were employed. In the following we will first discuss the principle of microtomography, then describe the different realizations of this method and present a number of promising results of its use in medicine and biology. Finally we will try to evaluate the development of μ CT and name eventual applications in the future.

There are two reviews in the literature which describe part of the older work (Graeff and Engelke, 1991; Kinney and Nichols, 1992). A third on biomedical applications of μ CT gives a brief overview of the field (Graeff, 1996).

II. PRINCIPLE AND TECHNIQUES OF X-RAY MICROTOMOGRAPHY

2.1. Projection and Reconstruction

By using tomography it is possible to determine the internal structure $s(x', y', z')$ of a specimen without the need for making a direct local measurement at each position (x', y', z') , which usually implies destruction of the sample by some mode of sectioning. Note that we use the coordinate system x, y, z which is fixed to the laboratory, and x', y', z' which is fixed to the sample (Fig. 1). The X-ray beam originates at the tangent point S and propagates along y . z is normal to the orbit of the electron storage ring serving as SR-source. z' is either parallel to z (as assumed in the following discussion) or parallel to x . In most cases $s(x', y', z')$ is the absorption coefficient $\mu(x', y', z')$ but, as we shall see below, it can also be the refractive index $n(x', y', z')$ changing the phase of the X-ray beam, or even dichroism $d(x', y', z')$ induced by an external magnetic field (Schütz *et al.*, 1987) which interacts with the polarization of the probing X-ray beam.

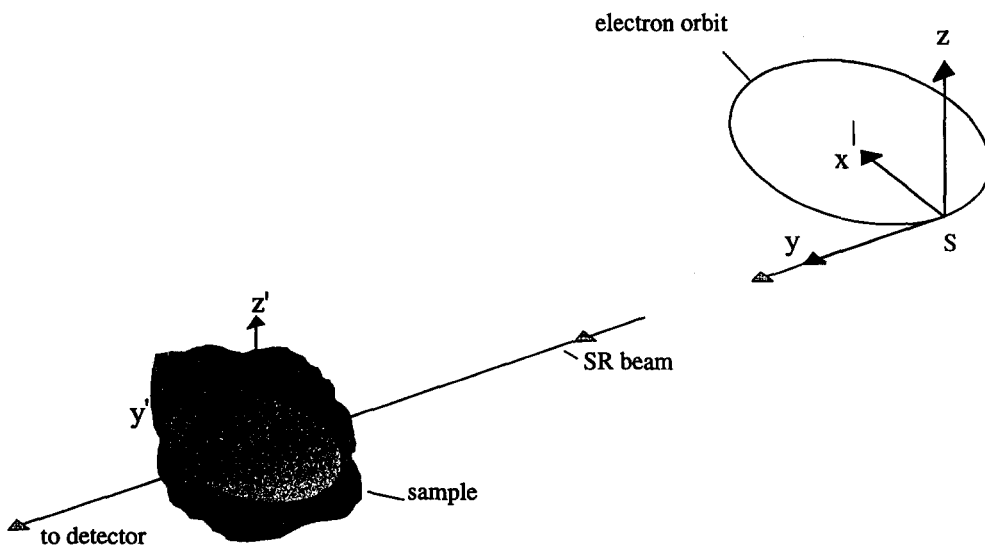


Fig. 1. The coordinate systems for CT using SRF: (x, y, z) fixed to the laboratory, and (x', y', z') fixed to the specimen. S: Tangent point from where SR is emitted.

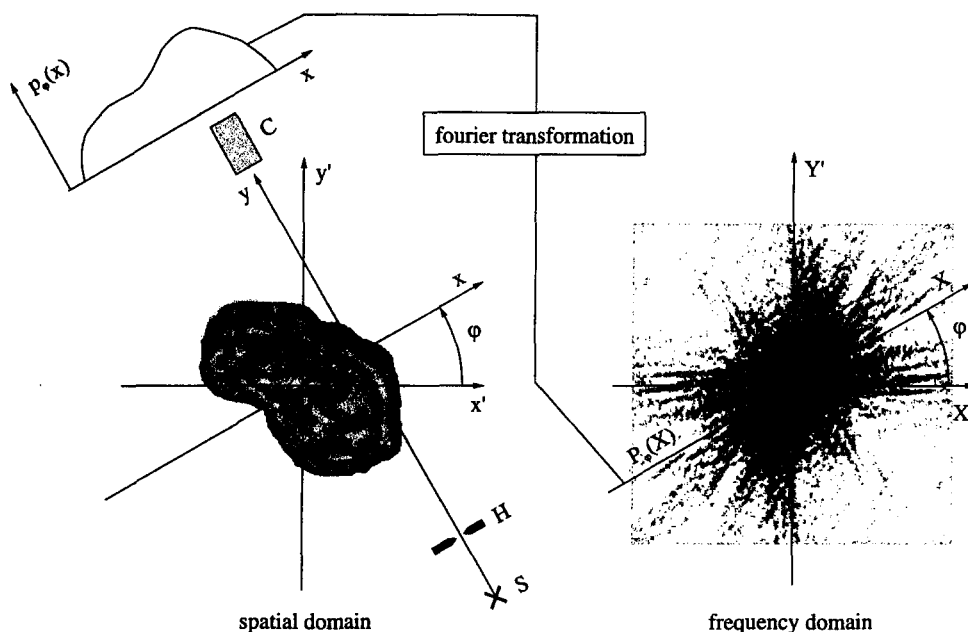


Fig. 2. At left: Single layer cut from the sample normal to the z -axis shown in real space. The shading represents the μ -density within this layer. S is emitting a well collimated beam, here indicated by the (with SR imaginary) pinhole H . C : Counter. $p_\phi(x)$ is the ϕ -projection recorded by C when the sample is scanned along x . At right: Frequency space. Shown is the two-dimensional FT $S(X', Y')$ calculated for the layer at left. The shading represents the weight of spatial frequencies present in the μ -density of the sample.

Let us imagine the specimen volume to be subdivided into a set of parallel slices normal to z' one of which is shown in Figs. 1 and 2. The principle of tomography is based on a mathematical theorem developed many years ago (Radon, 1917). Applied to our sample it says that a function $s(x', y')$ defined in any given slice of the set can be reconstructed from its line integrals taken at any direction in the slice. The 3D structure $s(x', y', z')$ of the sample is obtained by determining $s(x', y')$ for all z' and combining the results.

In order to formalize this statement we consider the tangent point S a point source. Because of the low divergence typical for SR it emits a pencil-shaped X-ray beam which is probing the sample. The pointbeam's position and its direction are defined by x and ϕ (Fig. 2). Behind the sample the beam intensity is registered by detector C . As sample structure $s(x', y')$ we take its absorption coefficient $\mu(x', y')$. The structure is implicitly contained in the photon count rates $N_\phi(x)$ at C , after combining them for all ϕ and x . Each $N_\phi(x)$ is determined by the line integral:

$$N_\phi(x) = N_0(x) \exp \left[- \int_{\text{beam}(\phi, x)} \mu(x, y) dy \right] \quad (1)$$

$N_0(x)$ is the number of photons incident on the sample. The integral is to be evaluated along the beam (ϕ, x) . A set of parallel beams is obtained by varying x while keeping ϕ fixed. In the experiment this means measuring $N_\phi(x)$ while shifting the beam in a direction parallel to the x -axis. The function

$$p_\phi(x) \equiv \left[\int \mu(x, y) dy \right] = -\ln[N_\phi(x)/N_0(x)] \quad (2)$$

is commonly called ϕ -projection. Introducing the δ -function, eqn (2) can be rewritten as

$$p_\phi(x) \equiv \iint \delta(x' \cos \phi + y' \sin \phi - x) \mu(x', y') dx' dy' \quad (3)$$

Eqn (3) is the Radon-transformation (RT) (Radon, 1917). It is the mathematical model

for measuring sample projections. The important point about the RT is that it implicitly contains the structure $\mu(x', y')$ which may be obtained explicitly if eqn (3) is solved for $\mu(x', y')$, as Radon was the first to show. To be successful one has to measure projections for many different directions φ . The determination of $\mu(x', y')$ from the x - φ manifold of measured projections $p_\varphi(x)$ is called image reconstruction.

There are a number of different reconstruction algorithms known in the literature (Kak and Slaney, 1987). They differ, among other aspects, in the projection geometry used. If, as in our case, synchrotron radiation is employed, then parallel projection as described above is the optimum choice and the reconstruction algorithm best adapted to this situation is the method of filtered back projections (BKFIL). Because BKFIL is widely used and, furthermore, lends itself for deriving an intuitive model of reconstruction, we describe it in the following (Kak and Slaney, 1987, p. 60).

Let

$$P_\varphi(X) \equiv \int_{-\infty}^{+\infty} p_\varphi(x) \exp(-2\pi i X x) dx \quad (4)$$

be the Fourier transform (FT) of $p_\varphi(x)$. $P_\varphi(X)$ is a plot in X - (i.e. frequency-) laboratory space of the occurrence of spatial frequencies X in the projection profile of the slice when viewed at "projection angle" φ defined in Fig. 2. A typical unit for X is lp/mm (line pairs per mm) when x is given in mm.

Furthermore, let

$$S(X', Y') \equiv \int_{-\infty}^{+\infty} \int_{-\infty}^{+\infty} \mu(x', y') \exp[-2\pi i (X' x' + Y' y')] dx' dy' \quad (5)$$

be the two-dimensional FT of the slice defined in (frequency) sample space X', Y' . $S(X', Y')$ is shown in Fig. 2 as a density map depicting the occurrence of space frequencies (periodicities) present in the slice. For example, the density at a point (X', Y') is representing how strong in the sample the periodicity is which has wavelength $\lambda = (X'^2 + Y'^2)^{-1/2}$ and direction parallel to the line from 0 to point (X', Y') . Applying simple geometry yields the angle enclosed by this line and the X' -axis as $\varphi = \arctg(Y' \lambda)$. The frequency density value $S(X', Y')$ is thus seen to be obtainable from $P_{\varphi_j}(X)$, the FT of the projection with angle φ , by setting $X = \lambda^{-1}$. This is the contents of the Fourier Slice Theorem (FST; Kak and Slaney, 1987, p. 56),

$$P_\varphi(X) = S(X \cos \varphi, X \sin \varphi) \equiv T(X, \varphi) \quad (6)$$

What this means is that $P_\varphi(X)$, the one-dimensional FT of the projection $p_\varphi(x)$, is identical to a central "cut" through the two-dimensional FT of the slice at angle φ .

The FST is the basic idea of reconstruction: after experimental determination of a large number of projections $p_\varphi(x)$ with different φ -values their FTs $P_\varphi(X)$ are calculated. Next the contributions of all "cuts" are superimposed to yield the complete function $S(X', Y')$ in frequency domain. Its re-transformation into real space then yields the structure. In polar coordinates this reads as follows:

$$\mu(x', y') = \int_0^\pi \left[\int_{-\infty}^{+\infty} T(X, \varphi) |X| \exp(2\pi i X x) dX \right] d\varphi \quad (7)$$

$x = x' \cos \varphi + y' \sin \varphi$ is the coordinate of the point (x', y') which it assumes when it is φ -projected. The factor $|X|$ arises when the area element $dX' dY'$ is transformed into polar coordinates according to $dX' dY' = X d\varphi dX$. Taking the modulus, $|X|$, allows for changing the φ -integration range from $[0, 2\pi]$ to $[0, \pi]$. Using eqn (6) we obtain

$$\mu(x', y') = \int_0^\pi \left[\int_{-\infty}^{+\infty} P_\varphi(X) |X| \exp(2\pi i X x) dX \right] d\varphi \quad (8)$$

The centre integral

$$q_{\varphi}(x) \equiv \int_{-\infty}^{+\infty} P_{\varphi}(X)|X|\exp(2\pi iXx)dX \quad (9)$$

is the mathematically exact description of the BKFIL algorithm. $q_{\varphi}(x)$ is the inverse FT of $P_{\varphi}(X)$, the FT of the original projection $p_{\varphi}(x)$, after applying the filter $|X|$ in frequency space. The filtering is not smoothening or an approximation but follows exactly from the transition to polar coordinates. Because of the shape of $|X|$ in frequency space the filter is called a ramp-filter. Combining eqn (9) with eqn (8) and substituting again $x = x'\cos\varphi + y'\sin\varphi$ we finally obtain

$$\mu(x', y') = \int_0^{\pi} q_{\varphi}(x'\cos\varphi + y'\sin\varphi)d\varphi \quad (10)$$

A measurement followed by reconstruction with the BKFIL algorithm consists of the following steps:

- (a) Scanning the beam along the x -axis, projections $p_{\varphi}(x)$ are measured in the range $[0 \leq \theta \leq \pi]$, e.g., 180 projections with increments $\Delta\varphi = 1^\circ$. In techniques employing an area detector the x -scan is replaced by simultaneous measurement. Furthermore, the intensity data at fixed φ are recorded simultaneously for a number of slices of the specimen (Fig. 3).
- (b) $P_{\varphi}(X) \equiv \text{FT}\{p_{\varphi}(x)\}$ are numerically calculated.
- (c) $q_{\varphi}(x) \equiv \text{FT}^{-1}\{|X| P_{\varphi}(X)\}$ are numerically calculated.
- (d) Back-projection of $q_{\varphi}(x)$. This means that for any x the value of $q_{\varphi}(x)$ is attributed to all points (x', y') of the slice for which the equation $x = x'\cos\varphi + y'\sin\varphi$ holds, i.e. all points on the "ray" of back-projection.
- (e) The structure $\mu(x', y')$ is the sum of all values attributed for the 180 different φ -values.

In the numerical calculation all integrals are replaced by sums. The ramp-filter $|X|$ is often multiplied with a low-pass filter function in order to reduce the noise in the tomogram.

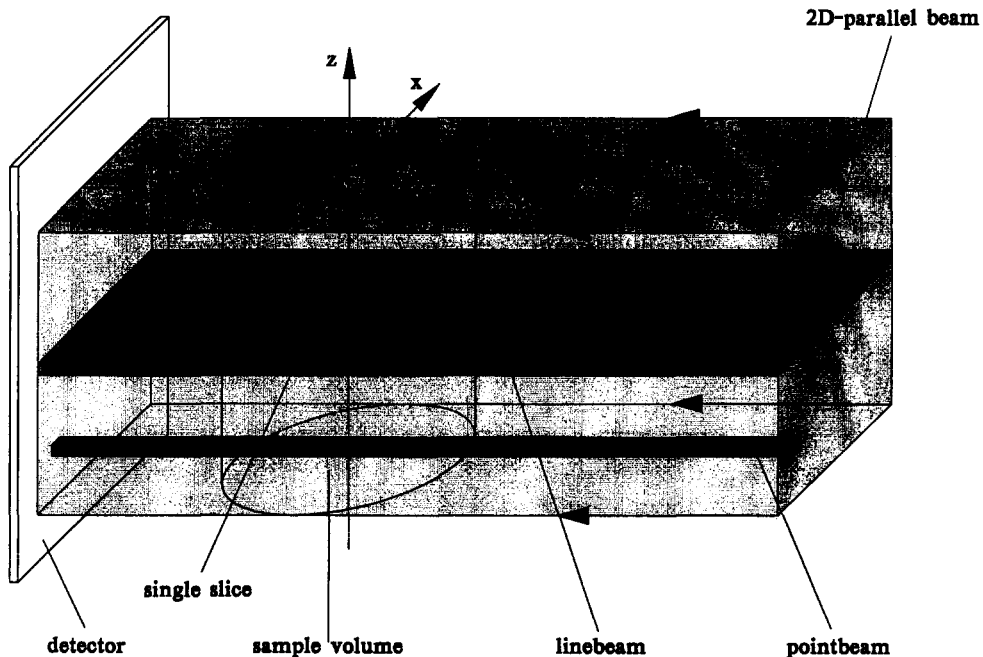


Fig. 3. Sketch of parallel projection of a cylindrical sample. Three kinds of beams are indicated: pointbeam, linebeam, and 2D-parallel beam.

2.2. Projection Modes

Besides the projection in parallel geometry assumed in the previous paragraph there are other possible arrangements mainly depending on the kind of source and detector used for a particular tomographic scanner. Two general beam geometries have to be considered: the parallelbeam (Fig. 3) and the conebeam (Fig. 4). A parallel set-up may be realized by a point, line, or "2D-parallel" beam, i.e. a beam with finite cross-section in the x - z -plane (Fig. 3) but at the same time practically zero divergence. A conebeam could be used in line mode (usually called fan beam) or with an area detector using the whole cone penetrating the sample.

2.2.1. Parallelbeam geometry

Figure 4 displays the different types of tomographic parallelbeam scanning.

2.2.1.1. Point scanning. A single pencil-beam travels through the sample and the transmitted fraction of the incoming beam is registered by a photon counting detector. In order to obtain the absorption index map of at least a single cross-section of the sample, a one-dimensional (1D) scanning of either the sample or the coupled source-detector unit must be performed. The scanning direction (x -axis) is perpendicular to the beam (y -axis) and the axis (z -axis) of rotation. The simplicity of this set-up is an advantage with respect to the costs of the scanner. Furthermore, the use of an energy resolving detector allows monochromatic registration of a polychromatic beam avoiding beam-hardening artefacts (see section 2.3.1) in the reconstructed image. Improving spatial resolution in point-scanning mode means simply reducing of aperture diameters and using smaller step sizes, which on the other hand leads to a corresponding loss of intensity, and therefore marks a serious disadvantage of the pointbeam technique. Scan times become very long and only a small portion of the incoming beam is used. If 3D information of a sample is required the point scanning is even more ineffective because additional scanning along the z -axis is required. If high spatial resolution is necessary, point scanning is not useful.

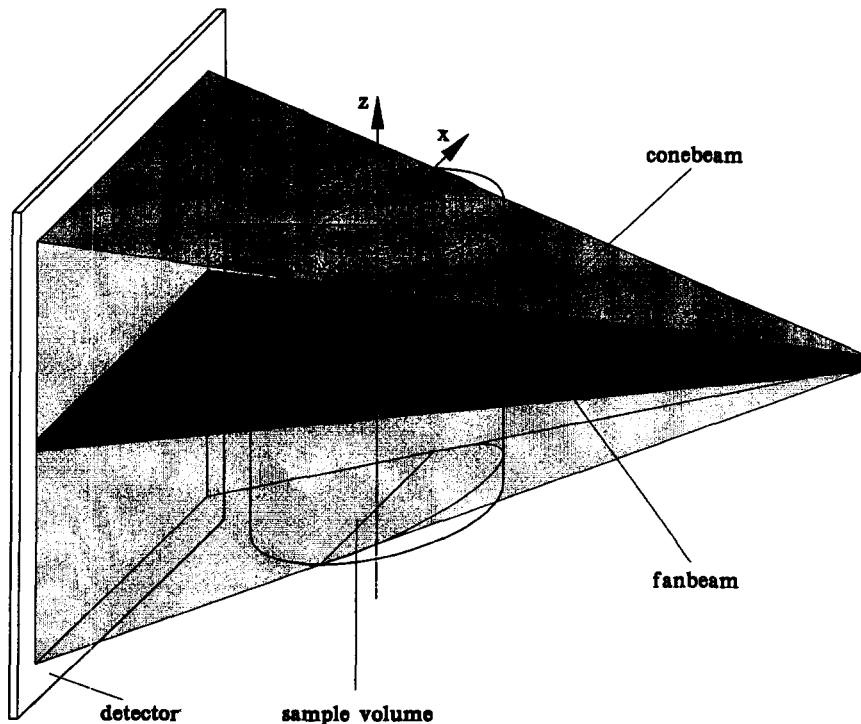


Fig. 4. Sketch of conebeam projection and fanbeam.

2.2.1.2. *Line scanning.* If a linear (1D) spatially sensitive detector is used, the absorption profile of one slice can be obtained within a single measurement if the detector array is aligned in x -orientation. In this case spatial resolution of the whole system relies on that of the detector. Depending on the size (p) of one pixel element and distance (d) to the detector, the collimation of the X-ray beam has to be better than p/d , a demand that can be met by geometries featuring sufficiently large distances (D) between photon source (of size s) and sample. This leads to the condition

$$s/D < p/d, \quad (11)$$

which implies a small source size and an appropriate large distance from the source. Due to this condition, conventional X-ray tubes applied to parallelbeam μ CT usually fail to make use of the major part of photon flux they generate, since at the desired distance only a small fraction of the whole cone is available for sample investigation. On the other hand, synchrotron radiation is by its nature collimated to a very narrow cone. This allows very large distances without considerable loss of intensity. Therefore SR is predestined for parallelbeam μ CT, providing spatial resolution capabilities of typically 0.1–0.3 μ m at usual SR beamlines. However, the line scanning geometry still requires scanning along the z -direction in order to investigate a 3D sample volume, i.e. time consuming slice-by-slice examination of the specimen has to be performed. This disadvantage can be avoided by using a 2D detector.

2.2.1.3. *Parallel projection.* To exploit best the whole cross-section of a 2D-parallel beam a 2D spatial sensitive detector array is necessary. A large number of slices may be investigated simultaneously, depending on how many rows the detector provides. Present CCD-based detector systems feature up to 2000×2000 pixels which saves scanning time by a factor of 4×10^6 when compared to point scanning. Routine measurements of 3D objects become feasible with these detectors with overall scan times ranging from minutes to hours instead of days or even weeks with line or point scanning geometries.

2.2.2. Conebeam geometry

The conebeam geometry is related to divergent, point-like sources. In order to effectively use their radiation one has to consider a diverging beam penetrating the sample. Although reconstruction algorithms for this geometry are more complex than with parallelbeams conebeam geometry is widely used since typical X-ray tubes belong to the mentioned class of sources. Figure 4 displays the ray geometry in conebeam projection. Scanning a pointbeam is unusual in the cone geometry because the use of a single probing beam suggests it is just as well to employ parallel geometry (e.g., by moving the sample or the whole source detector unit) thereby avoiding the numerically more involved cone- or fanbeam reconstruction techniques.

2.2.2.1. *Fan scanning.* This geometry is widely used in medical CT scanners. A linear array of detector elements is placed opposite to the source. Both are rotated stepwise around the patient. In the case of μ CT investigations the small sample is rotated in the divergent fan beam of the X-ray source. An advantage of this set-up is the magnifying characteristic allowing high-resolution imaging with medium-resolution detectors. The spot size of the source limits spatial resolution. In order to obtain a homogeneous distribution of beam directions it is necessary to rotate the sample for a whole 360° turn. If 3D information is desired this set-up again requires linear scanning along the axis of rotation, and time consuming slice-by-slice examination of the object has to be performed.

2.2.2.2. *Cone projection.* Besides employing a 2D detector, a more sophisticated reconstruction technique must be applied if the whole cone of X-rays shall be used. Reconstruction no longer separates into independent data sets of slices, which is only true for one central plane, where the whole fan of X-rays is perpendicular to the rotational

axis. All the neighbouring slices are penetrated at an angle increasing with the distance from the central slice. Several 3D or conebeam algorithms have been developed which solve this problem and generate a 3D set of data from the cone projections taken by 2D detectors (Feldkamp *et al.*, 1984; Kak and Slaney, 1987, p. 99ff).

2.3. X-Ray Sources and Detectors

This paragraph focuses on characteristics of sources and detectors for X-ray imaging. Among the first applications of X-rays after their discovery by Wilhelm Conrad Röntgen 100 yr ago was medical imaging of a human skeleton. Since then developments in the medical field were aimed to optimize image quality and speed and to minimize dose. In many sciences the capability of X-rays to penetrate matter opened up a wide range of applications among which obviously imaging plays the most dominant role. With respect to efficiency, sensitivity, spectral and spatial resolution, types and parameters of detectors are closely related to certain characteristics of the sources. Therefore source parameters like flux, wavelength spectrum, angular distribution of emitted radiation, and source size are important data for devising and optimizing imaging techniques.

2.3.1. X-Ray sources

In X-ray tubes, X-rays are generated by stopping fast electrons in a target material inside an evacuated glass tube. The energy of the X-ray photons is of the order of the electron energy. The electrons' acceleration voltage determines the upper limit of emitted X-ray energy. X-Rays produced by this principle are called Bremsstrahlung. Their spectrum is a white continuum. In addition, there is a characteristic line spectrum of X-rays arising from atomic excitations of the target material. With a proper choice of target material and accelerating voltage, the peak intensities of the sharp characteristic lines can be made comparable to the Bremsstrahlung intensity or to exceed the latter by orders of magnitude.

One component in securing high image quality is how well the source spectrum is adapted to the given composition of the sample. A general rule is that the energy of X-rays must be higher if samples are thicker or more dense than others. Absorption contrast is improved by varying the acceleration voltage for the electron beam and/or using filters. The best choice of energy will be discussed in section 2.4.1. A secondary and rather troublesome effect of the absorption varying with energy is beam-hardening (Kak and Slaney, 1987, p. 117; Beckmann, 1993; Günnewig, 1996). A consequence of the energy dependence of absorption is that the spectrum of any X-ray beam changes while it penetrates a given sample. Low energy parts of the beam are stopped earlier on the way through the sample and high energy parts can more easily pass the whole object. The high energy side of the spectrum is therefore preferred with respect to the low energy region after penetration of a sample. Unfortunately beam-hardening cannot easily be corrected for by mathematical methods because it depends both on material composition and path length through the sample. Some approximate correction methods are known for objects consisting only of very few different materials. Another approach for avoiding beam-hardening errors is measuring independently with two different X-ray spectra ("dual energy" method). The only way to principally avoid beam-hardening is to use monochromatic radiation. Bragg reflection by a crystal or fluorescence excitation of X-rays are common ways to eliminate unwanted energies from the spectrum. The monochromatic incident beam is generally several orders of magnitude less intense than the polychromatic beam. As a result data acquisition becomes very slow, especially when high spatial resolution and/or low noise images are wanted.

X-Ray flux from tube sources is limited by the thermal load of the electron beam hitting the anode material. Even with rapid water cooling a tube target with a focus area of typically 10–20 mm² never sustains substantially more than about 200 W/mm² specific dissipated heat. This holds for a high melting target material like W or Mo and is accordingly less for targets of Ag, Cr or Fe. Water-cooled tubes with rotating anodes

stand roughly a tenfold higher specific thermal load. Fine and very fine focus tubes may exceed these per area values by another factor of 5–10 but, integrated over their radiating source area, have a correspondingly smaller X-ray flux. Nevertheless such tubes with spots down to 2 μm diameter have been designed and can be useful when the source size is the decisive parameter determining spatial resolution of the image.

Another approach of X-ray production is principally similar to X-ray tubes but employs an electron microscope and its capability of supplying a well focused electron beam inside a vacuum chamber. X-Ray target (anode), sample, and the whole imaging system are positioned inside a scanning electron microscope (SEM) (Thomas *et al.*, 1992; Fuhrmann, 1993). The electron beam is focused on the exchangeable target allowing for different X-ray spectra without changing tubes or sample. No X-ray tube with glass, exit windows and external shielding are needed. A certain disadvantage can be the location of the whole system inside a vacuum chamber which makes it inaccessible during measurement. This disadvantage can be avoided by providing a separate sample chamber at atmospheric pressure or appropriately reduced pressure to at least reduce the scattering of X-rays (Thomas *et al.*, 1992).

With the advent of SR a novel kind of X-ray source became available. SR has some really outstanding features which make it interesting for imaging applications in various fields. Synchrotron radiation originates from accelerated charged particles similar to the Bremsstrahlung of X-ray tubes. However, in this case the acceleration is not performed by stopping a linear motion of electrons but by maintaining circular motion of charged particles in storage rings. Electrons or positrons circulate very close to the speed of light at energies of some GeV. Due to relativistic effects the direction of radiation emission is not symmetrical to the direction of acceleration but is tangential in forward direction with respect to the path of the electrons. The angular distribution of the photons is restricted to a very narrow cone the divergence of which decreases inversely proportional to the electron energy. With particle energies between 1–6 GeV beam divergence varies from 0.5 to 0.085 mrad.

The spectral distribution of SR is a broad white band, beginning with IR through visible and UV up to soft and hard X-rays. The upper limit of energy depends on the electron energy.

As a common parameter of the SR spectrum the critical Energy E_c is given as the value of the spectrum dividing it into two parts with equal integral energy content. One finds

$$E_c \sim E_e^3/R \quad (12)$$

E_e is the electron energy and R the radius of curvature of the electron path. Or, in order to give a numerical example, if E_c is given in [keV], E_e in [GeV] and R in [m] we have

$$E_c = 2.218 E_e^3/R \quad (13)$$

For the storage ring DORIS at DESY (Hamburg, Germany) with $R = 20$ m and particle energy of $E_e = 4.5$ GeV the critical energy E_c determining the spectrum would be 10.11 keV.

The electrons are forced to their circular path by dipole magnets with magnetic fields oriented perpendicular to the electron orbit. A storage ring has typically several curved sections with straight sections in between. The magnetic dipole is called bending magnet, and since inside the dipoles in which SR is emitted we speak of bending-magnet sources.

In order to obtain higher energies of X-rays, the spectrum can be shifted to shorter wavelengths by increasing the dipole field. In addition, the intensity of SR can be multiplied by letting the electrons run through a number of dipoles behind each other with alternating sense of curvature. In such a device, usually called a wiggler, the intensity of the radiation is amplified by the superposition of the beams originating at the individual wigglers. If electromagnets are used, the magnetic field can be adjusted by the current of the coils and thereby the spectrum and the intensity of the wiggler may be tuned according to the requirements of the experiment. With permanent magnets the magnetic field can

still be varied by changing the gap between the magnetic poles. The determining parameters of a wiggler are the peak magnetic field B_0 at the electron orbit and the period length λ_w of the magnetic field along the electron path. By these values a quantity K is defined:

$$K = \frac{\lambda_w e B_0}{2\pi m_e c} \quad (14)$$

If K becomes smaller than unity the device is called an undulator. The essential point making undulators different from wigglers is that for a single electron the emission of photons at different wigglers is coherent. While with wigglers the divergence of the emitted beam is of the order of $2.0 \times 0.1 \text{ mrad}^2$ (horizontal \times vertical; ID11 at the ESRF, Grenoble, France) with undulators this is reduced to about $0.2 \times 0.04 \text{ mrad}^2$ (ID13 at the ESRF). A wiggler has a broad band continuous spectrum. The wavelength spectrum of an undulator has line form preferring certain energies. The spectrum can be adjusted by varying the undulator gap. This feature allows pre-monochromatization of the X-ray beam and a more efficient exploitation of the produced flux of X-rays.

The main advantages of SR over X-rays from X-ray tubes are: high intensity and/or brilliance, collimation, tuneability over a wide wavelength spectrum, linear or elliptical polarized radiation. Brilliance is defined as number of photons per (time, source area, solid angle, relative bandwidth, electron current). Brilliance and photon flux (brilliance \times source area) are many orders of magnitude larger than those of the characteristic lines of any X-ray tube. Thus monochromatization with extremely high photon fluxes at the sample is achievable, which is very useful in numerous applications and especially for imaging purposes. X-Ray monochromators are typically Bragg reflecting single crystals. With a fixed incident Bragg angle θ_B a set λ_n of wavelengths is selected from the continuum according to

$$\lambda_n = 2(d/n)\sin\theta_B \text{ with } n = 1, 2, 3... \quad (15)$$

Here d is the Bragg plane spacing belonging to the fundamental wavelength λ_1 . λ_n with $n > 1$ are higher order reflections and called harmonics. Other wavelengths are not reflected by the crystal but are, except for absorption, transmitted through the crystal. The harmonics prevent the ideal monochromatization but can, if necessary, be suppressed by slightly detuning the two crystals of the double-crystal monochromator. The latter is the most common monochromator arrangement at SR beamlines. The spectrum is tuned by rotating the monochromator crystals with respect to the incoming beam.

Using monochromated X-rays beam-hardening effects can be avoided completely. The spectral tuneability allows adaptation of the wavelength to material composition and size of a given object. High intensity is necessary for performing routine investigations in a reasonable time. This is already true in the case of tomography in general since it requires a large number of projections to be taken in a single investigation. Large flux is an even more important requirement in the case of μ CT, i.e. when high spatial resolution is required, because the number of photons needed for a certain image quality rises at least proportionally to w^{-4} , where w is the length scale of image resolution, see eqn (22) below.

Furthermore, spectral tuneability enables the identification of specific components in a given sample by exploiting the absorption characteristic of the elements or even that of chemical binding states. For a more detailed description of such methods see section 2.4.2.

In order to make full use of the spatial resolution capabilities of SR imaging, geometries different from those used with X-ray tubes are necessary. Due to the extremely low divergence of SR, beam projection imaging can be employed at a sufficiently large distance from the source. By placing the sample close enough to the detector image blur can be made negligible. Thus SR can provide X-rays for high resolution, high quality imaging in parallel-beam geometry. To exploit this capability correspondingly sophisticated area detectors of high spatial resolution are required.

2.3.2. X-Ray detectors

The ideal detector for X-ray imaging should meet all of the following requirements: every incident photon of the complete band of X-ray energies is detected (efficiency, spectral sensitivity), the response is linear over a large range of intensities (linearity, dynamic range), and the detector's spatial resolution matches that of the source (spatial resolution). Furthermore, if the device is designed for digital readout, the time for readout, digitization and data storage has to be short. In addition to this, for some applications one might want the detector to provide energy discrimination of the detected X-rays.

In order to "see" an X-ray image, X-rays have to be converted to visible light. Photon detection in the X-ray range is usually based on the photo effect and following reactions. The energy of the photon is completely absorbed by an electron which was bound either by a single atom or in a molecule or crystal. The excited system may release its energy by either emitting photons as a secondary effect or by radiation-less transitions to the ground state. Depending on the material composition mixtures of these processes in a cascaded scheme are possible. The primary X-ray is detected mainly by secondary photons or electrons.

For X-ray imaging various types of scintillation detectors are in use. Such devices are characterized by the first conversion step in which they use materials called scintillators for converting X-rays to light. Figure 5 shows a typical set-up of a spatially sensitive X-ray detector (Busch *et al.*, 1995) which is described here as exemplary for a variety of similar systems, the special features of which are mentioned afterwards. A 2D flat scintillation screen converts the X-ray image into a visible light image, which might be observed by eye. To obtain a quantitative signal in digital form the optical image is projected by a lens system to a CCD chip where the light is converted to an electrical signal for each picture element by means of an analogue digital converter (ADC) and stored to computer disk memory for further evaluation.

The properties of the conversion screen substantially determine the quality of the detector. Spatial resolution and efficiency, especially, are determined by the type of screen employed. As a general rule the screen should be thin and homogeneous to provide good

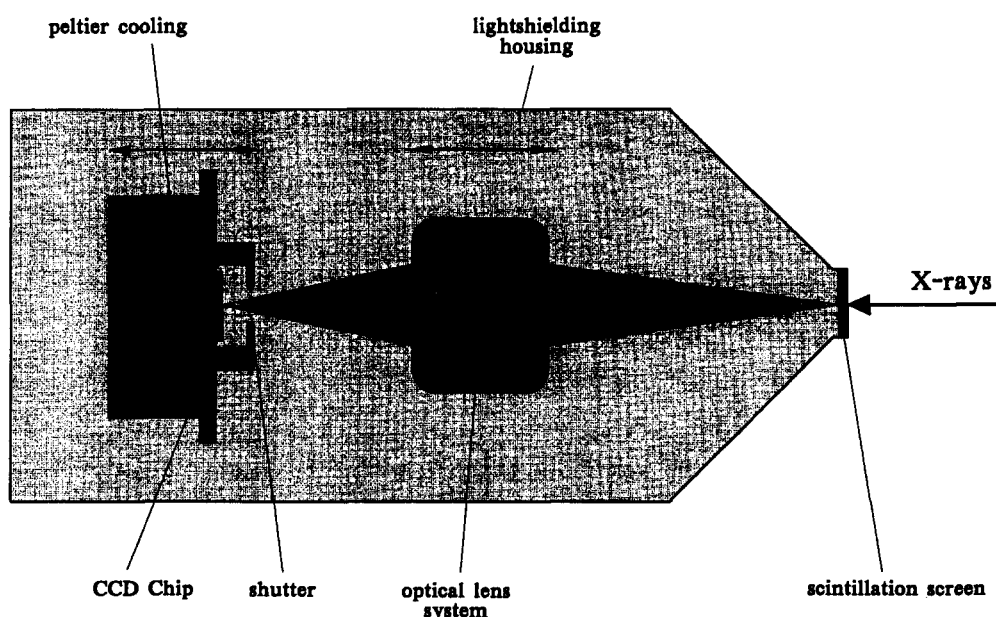


Fig. 5. 2D X-ray detector consisting of scintillation screen, optical lens system, and CCD chip which is peltier-cooled. Different magnifications of the primary image can be realized by remote adjustment of lens and chip as indicated in the figure. Note that the scintillation screen does not move when magnification is changed. The entire unit is tight against visible light from the outside.

resolution, but a better efficiency requires a thick scintillating layer. Two different kinds of screens are in use: the majority of screens employ polycrystalline layers of scintillator material made up of a scintillation powder fixed to a substrate by a transparent binder. For some high resolution applications single crystal screens are used which provide superior spatial resolution due to almost no scattering of visible light within the scintillation layer. On the other hand, single crystal screens have poor efficiency because due to refraction of the light cone when it leaves the screen only a smaller portion of it can be accepted by the lens system.

There are various scintillator substances to choose from to match requirements of the particular application, such as X-ray spectrum and intensity to be recorded, the spectral response characteristic of the light detector, its speed, and the radiation dose to be handled. Commonly used powder scintillators are CaWO_4 , CsI(Tl) , CsI(Ba) , $\text{Y}_2\text{O}_3\text{:Eu}$, $\text{Gd}_2\text{O}_3\text{:Tb}$, and $\text{ZnCdS}_2\text{:Ag}$. As single crystal scintillator screens, BGO ($\text{Bi}_4\text{Ge}_3\text{O}_{12}$) and CdWO_4 are employed.

The lens system has to transfer the optical information to the detecting CCD. Important requisites for this process are efficiency and precision in order to make best use of the information contained in the visible image. The lens system should therefore be optimized both for speed and definition. In real optical systems these requirements are contrary. A compromise has to be made in which one tries to consider adequately the main demands of the imaging application. The balancing parameter is the diameter D of the optical aperture stop. Its ratio to the focal length f , D/f , can be changed by an iris diaphragm at the lens. The scale and thereby the field of view can be varied by sliding the lens and CCD detector along the optical axis of the system. The system shown in Fig. 5 uses a $f = 50$ mm lens and is capable of magnification scales from 1–6.

For the detection of visible light mainly CCD chips and photodiode arrays are employed. Video tubes are rarely used. Outstanding features of CCDs are their linear responses, extending up to a dynamic range of 10^5 , their ability to stay unaffected by overexposures, and their operability in integrated mode for up to several hours if sufficiently cooled. The detection principle is based on semiconductor capacitors as picture elements, collecting the electrons generated as electron-hole-pairs by incident photons. After integration, the pixel charges are transferred to a readout register on the chip and serially read out for ADC processing so that the signal can be evaluated by computers. Quantitative tomographic image evaluation requires precise digital image conversion of the input projections. Accordingly digitization by 8–16 bit ADCs is meaningful for μ CT. The detector described here is equipped with a Kodak KAF-1400 CCD with 1320×1035 square picture elements of $6.8 \mu\text{m}$ size each. For each pixel 12 bit ADC conversion is supplied. A three stage peltier cooling system keeps the chip at -45°C thus permitting exposure times of several minutes at negligible dark current.

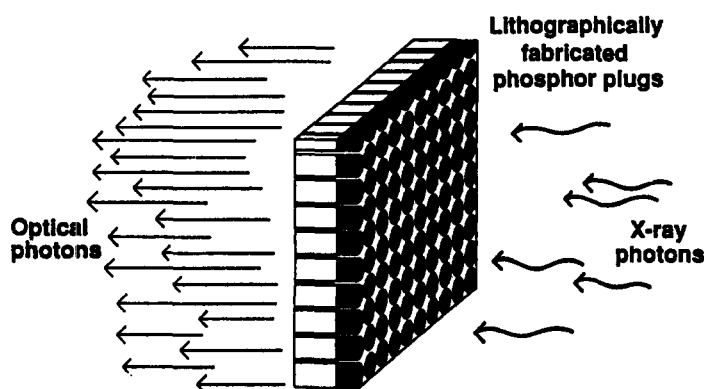


Fig. 6. Schematic of the cellular phosphor plate. Reprinted with permission from Flannery *et al.* (1987).

There are variations of the described detector type in the literature. (Engelke *et al.*, 1989a; Takeda *et al.*, 1994; Kinney and Nichols, 1992; Nagata *et al.*, 1992; Thomas *et al.*, 1992; Fuhrmann, 1993; Feldkamp *et al.*, 1989; Flannery *et al.*, 1987; McNulty, Kirz *et al.*, 1992; Castelli *et al.*, 1994). Depending on the applications these detectors are used as they vary in size, resolution, efficiency, and flexibility. The choice of scintillation screen influences size (field of view), resolution, and efficiency. A special type of scintillator has been developed (Flannery *et al.*, 1987; Castelli *et al.*, 1994) based on the discrete structure of a fibre optic face-plate with scintillator coating of every single fibre end (Fig. 6). Such scintillators minimize cross-talk between different scintillator cells of the scintillation layer and yield good spatial resolution while maintaining efficiency by direct optical coupling to the fibres.

The optical coupling between the scintillator and imaging device can be performed by different methods. The projection by a lens system as described above is widely used (Takeda *et al.*, 1994; Kinney and Nichols, 1992; Flannery *et al.*, 1987; Busch *et al.*, 1995) and offers high spatial resolution combined with large flexibility of magnification. These features are paid for by reduced efficiency, because only a relatively small fraction of the scintillation light is caught by the objective. In order to overcome this drawback, detectors with fibre-optical coupling have been developed (Engelke *et al.*, 1989a; Nagata *et al.*, 1992; Thomas *et al.*, 1992; Fuhrmann, 1993; Castelli *et al.*, 1994), yielding high efficiency at fixed magnification and resolution. Direct coating (McNulty, Kirz *et al.*, 1992a) of a CCD by a scintillation layer is only useful with soft X-rays because high energy X-rays damage the CCD.

Another 2D detector type (Suzuki *et al.*, 1989) based on a pickup tube is being used for X-ray imaging. The faceplate of the tube (Fig. 7) is designed translucent to X-rays by combining a 500- μm Be window glued to the atmospheric side with the 25- μm glass wall of the tube at the vacuum side. This arrangement guarantees high X-ray transmittance and also stability against atmospheric pressure. The X-ray sensitive layer consists of an amorphous Se/Al alloy and is 20 μm thick. It is read out by scanning with an electron beam yielding a current modulation proportional to the X-ray intensity. The output signal is converted to digital data for further processing by the computing system.

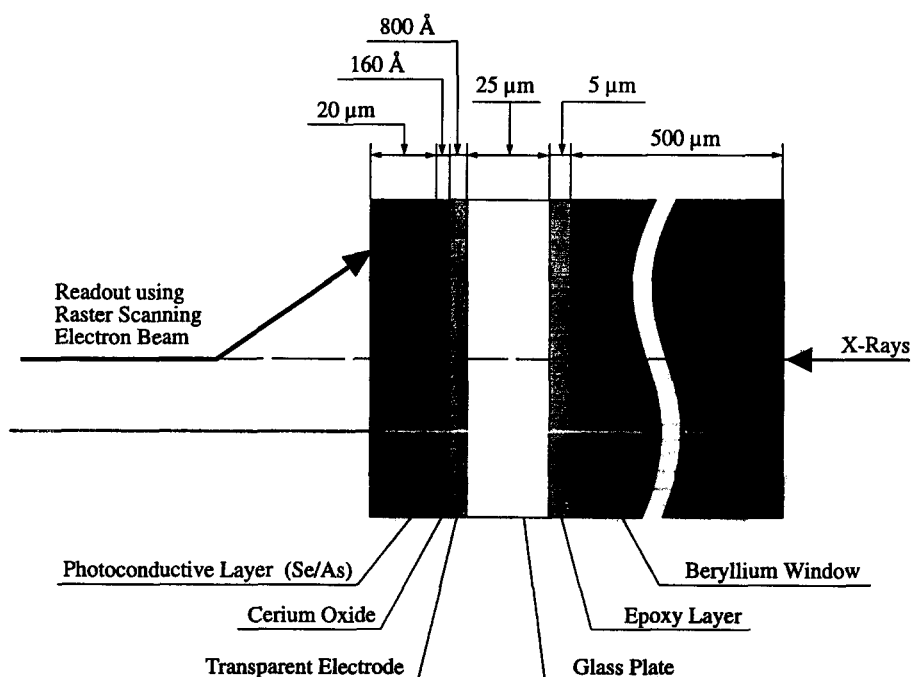


Fig. 7. Faceplate structure of pickup tube (after Suzuki *et al.*, 1989).

The detectors described above are not energy resolving. Charges collected in time-integrating CCDs and pickup-tube currents can no longer be assigned to the individual X-ray photons they originate from. The resulting signal is therefore proportional only to the product of energy and number of collected photons and not to the photon energy alone. By now there are no 2D detectors available that feature high spatial resolution and energy resolution at the same time. If for a given application a good energy definition is required one can either employ a 2D detector combined with monochromatic X-rays to avoid the need for energy resolving detection, or combine microbeam and sample scanning and use the energy resolving zero-dimensional detector (Borodin *et al.*, 1986).

Scintillation counters provide medium energy resolution (20–50% in the X-ray region). They consist of a scintillation crystal optically coupled to the photocathode of a photomultiplier tube which finally outputs a voltage pulse proportional in size to the energy of the incident X-ray photon. The energy dispersion of this counter can be used to avoid beam-hardening effects even with a white spectrum of incident photons. Energy resolution on the percent level is achieved with semiconductor counters (SSD). They are especially useful for spectroscopic applications.

As stated above, scintillation screens currently limit the spatial-resolution capability of tomographic systems. To get around this restriction X-ray optical pre-magnification (Bonse *et al.*, 1986; Suzuki *et al.*, 1990; Nagata *et al.*, 1992) can be used. X-Ray magnification is achieved by asymmetric Bragg reflection (Fig. 8). As shown in eqn (15) this kind of reflection is not a surface reflection but is due to the Bragg planes of the crystal volume beneath the surface. The reflecting planes are not necessarily parallel to the surface and thereby the incident and reflected beam must not be symmetrical with respect to the surface. For geometrical reasons a small incidence angle combined with a steep reflection angle results in widening the beam. This effect can be used to magnify an X-ray image by interposing the asymmetric Bragg reflection between sample and detector.

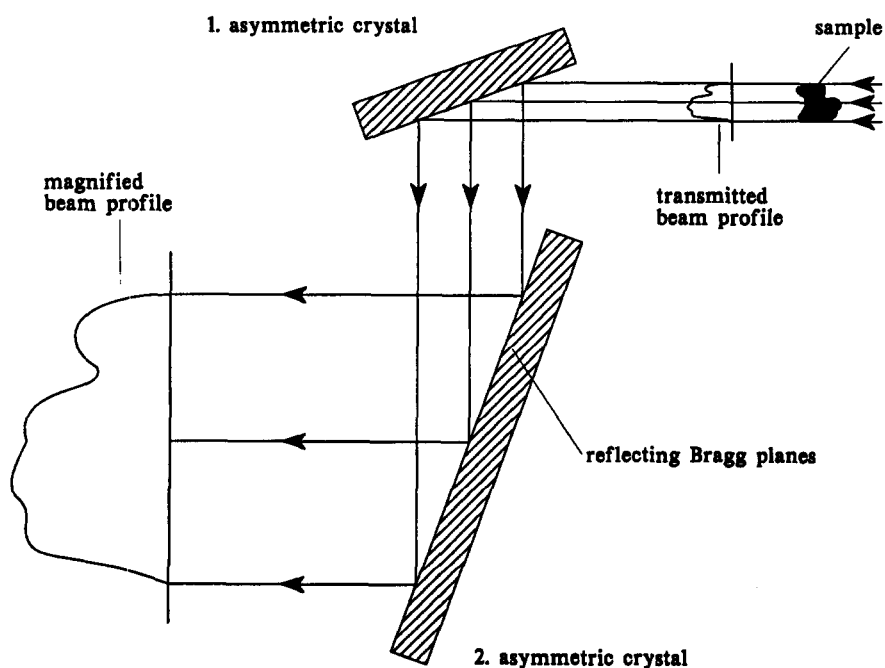


Fig. 8. X-Ray optical magnification by two-fold asymmetric Bragg reflection. For optimum transmission the Bragg planes of the crystals must be tilted with respect to each other by a small angle of the order of 1–10 μ rad (after Nußhardt, 1990).

2.4. Contrast Mechanisms

Image contrast originates from any modulation of the probing radiation. The sample can absorb, scatter, reflect, diffract, and phase-shift the investigating beam. Depending on radiation characteristic and sample composition several effects may occur simultaneously. X-Ray imaging primarily uses absorption contrast which is discussed in section 2.4.1. Some approaches to employ other effects are under development, e.g., the use of Compton scattering, of fluorescent radiation, of diffracted X-rays, and of phase shift. The latter case shall be discussed below (2.4.2) because X-ray phase contrast promises to be complementary to normal absorption contrast which fails to distinguish between low density materials consisting of light elements. Phase-contrast is considerably more sensitive to compositional changes in low-Z materials than is absorption contrast since the latter varies approximately with Z^4 whereas phase-contrast varies proportional to Z . A more detailed discussion will be given in section 3.5 below.

2.4.1. Absorption contrast

Absorption mechanisms relevant in the X-ray region are the photoelectric and the Compton effect. With photoelectric absorption the incident X-ray photons energy is completely transferred to a core electron of the absorbing atoms. The electronic excitation energy is emitted by secondary processes (i.e. auger electrons, fluorescence photons), which mostly do not contribute to the detected image signal. The Compton effect is the scattering of the incident photon at one atomic electron, resulting in a scattered photon with lower energy and the electron taking the remaining energy. The electronic energy is again not likely to be observed, whereas the Compton scattered photon has a considerable probability to be scattered by small angles and can therefore be detected at erroneous positions in the detector. This leads to a scattering background in the projection. The impact of both interactions to the incident X-ray beam is characterized by the linear absorption coefficient $\mu(x, y)$, from eqn (2), as exponential attenuation of X-rays.

Tomographic and radiographic imaging with X-rays reveal the spatial distribution of μ within the object. Image contrast arises from variations of μ within the sample material. Radiographic images display the projection $N(x) = N_0(x) \exp(-\int \mu(x, y) dy)$ of the integrated attenuation coefficient along the path of the X-rays travelling through the sample. Tomographic data are usually expressed as a dimensionless array of $w \cdot \bar{\mu}(x, y, z)$ values with the voxel size w and the mean absorption coefficient $\bar{\mu}$ of the voxel volume at the array position (x, y, z) . This distribution map of μ values can be interpreted as a coarse approximation of the density distribution of the given sample and therefore allows to distinguish different materials by X-ray absorption tomography.

The absorption coefficient depends strongly on energy: $\mu = \mu(x, y, z, E)$. For X-rays the energy dependence is dominated by the photo effect and in the region between two absorption edges is approximately described by the Jönsson formula (Jönsson, 1928)

$$\mu \sim (Z \cdot \lambda)^m \text{ with } 2.5 < m < 3.5 \quad (16)$$

This relation implies beam-hardening if a polychromatic beam penetrates a sample as described in section 2.3.1. Figure 9 displays as an example of beam-hardening the absorption profile through a homogeneous sample of Al (Günnewig, 1996). The measurement was performed using a Mo-target X-ray tube (continuous line) and the same tube with an additional 120- μm Zr filter (dashed line). It is clearly seen that after reconstruction absorption values in the centre of the sample are too low. The effect is less severe if a spectrum which is narrowed by a suitable filter is used (dashed plot).

Energy dependence of absorption can be used to minimize scan time for a given sample. To accomplish this one selects the energy to match elemental composition and diameter of the object. In order to achieve a certain sensitivity $\Delta\mu/\mu$ of measurement, the energy has to be chosen high enough to ensure a sufficiently large number of X-rays to penetrate the sample in acceptable time. If the energy is too large, only few photons are absorbed and therefore the sensitivity for small changes in μ decreases. The optimum condition for

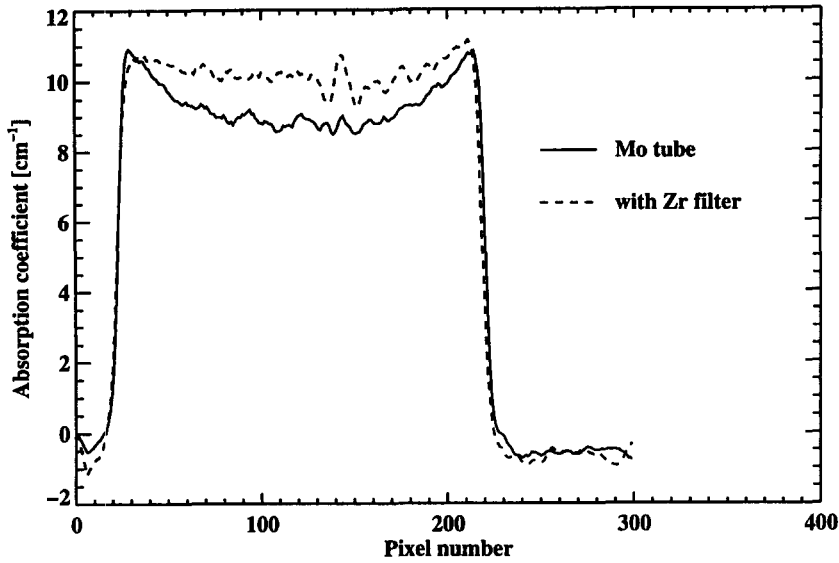


Fig. 9. Beam-hardening profile of an homogeneous Al specimen. With polychromatic radiation (Mo tube) the centre part appears of lower density than the outer region. Using chiefly Mo-K α radiation (Zr filter) this error is much reduced.

minimizing scan time at any prescribed sensitivity is given by the relation

$$\mu(E) \cdot D = 2 \quad (17)$$

D is the sample diameter. Equation (17) was derived by Grodzins (Grodzins, 1983) based on a model of photon counting statistics in CT by Chesler *et al.* (Chesler *et al.*, 1977). It helps making the best choice of energy for high contrast and minimum observation time.

X-Ray absorption-images reveal a large amount of quantitative structural information. Fortunately, in most applications this information is little troubled by the principal image errors which can usually be made negligibly small by arranging the experiment in a suitable way. However, two types of errors and typical situations in which the general statement does not hold should be discussed here. One is beam-hardening as already described in section 2.3.1 and displayed by Fig. 9. Beam-hardening can easily be prevented by employing monochromatic SR. The other is the deflection of X-rays by scattering, refraction or reflection at the surface or in the bulk of the sample. We shall consider this effect next.

Scattering of X-rays is one source of image degradation leading to a raised background. If this background is constant within the image region, only the contrast is slightly reduced. For high definition imaging such background can be significantly depressed by the use of a crystal collimator between sample and detector (Takeda *et al.*, 1994).

The effect of X-ray refraction and reflection plays a greater role since it depends on the orientation of sample surfaces with respect to the X-ray beam. Although the refractive index of material at X-ray energies is very close to unity, the angular deviation of X-ray beams due to refraction and/or reflection at or near the specimen surface can be significant. Assuming a typical refractive index of $n = 1 - 5 \times 10^{-6}$, the maximum angle of total reflection is 0.36° and thus big enough to impair spatial resolution. The effect becomes particularly severe when collimators are applied because the deviated beams can fail to be transmitted by the collimating system and appear as if they had been absorbed by the sample. When the sample is rotated on recording projections, the pretended absorption changes in magnitude so that the same voxel elements seem to vary during a tomographic scan which is the cause of artefacts in the reconstruction. The error becomes even more important at increased spatial resolution. Especially if X-ray optical pre-

magnification is employed as described at the end of section 2.3.2, refraction and reflection at the surface can be troublesome because magnifying crystals are also very sensitive to small changes of incident angles and act therefore as strong collimators.

2.4.2. Differential absorption contrast

The absorption formula of Jönsson (eqn 16) indicates an increase of μ approximately with Z^4 (Z is atomic number), which reflects the close correlation of absorption and sample density. At the absorption edges the Z^4 dependence is superimposed with characteristic structures in the shape of sudden increases of absorption with raising energy. Whenever the X-ray energy exceeds an ionization level, an additional electron contributes to photoelectric absorption of the atom and therefore suddenly increases the otherwise decreasing absorption coefficient. Due to the different electronic configurations of the elements the edge energies and heights are not the same for different elements.

This fact in combination with a tuneable X-ray source like SR allows to clearly discriminate the distribution of single elements within a sample by differential measurement. To this end two tomographic scans are performed at energies right below and above the absorption edge of the desired element. Taking the difference yields only the contribution of this one element, since for the remaining elements the change in absorption is negligibly small. Applying this method to samples containing elements with neighbouring Z values one can clearly distinguish separated distributions of either desired element (Bonse *et al.*, 1989; Nußhardt *et al.*, 1991).

The energy resolution of double crystal monochromators is about $\Delta E/E \approx 10^{-4}$. This value is small enough to facilitate not only elemental mapping but also to exploit the fine structure of absorption edges for separating different chemical states of the same element. Figure 10 (Johnson *et al.*, 1986) displays the normalized absorption near the K-edge of Fe. The fine structure of pure Fe differs from that of Fe_2O_3 due to different binding states of the Fe valence electrons. If for X-ray imaging an appropriate pair of energies is selected then the difference of the absorption fine structure changes sign and becomes large enough to map the chemical states separately. In this example Fe and Fe_2O_3 can be precisely distinguished by using the difference of images taken at E_1 and E_2 .

The method of differential absorption contrast is among the most outstanding possibilities of SR. Detailed 3D information about the chemical composition of samples

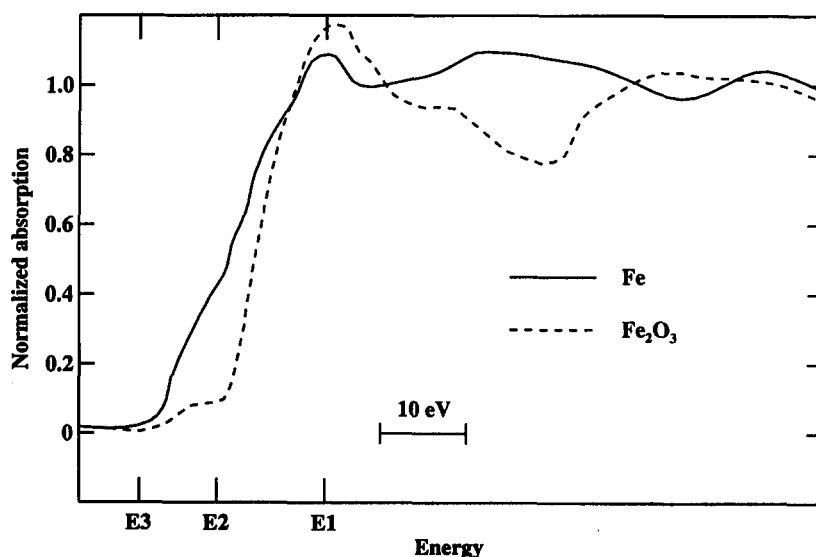


Fig. 10. Different absorption fine structure at Fe K-edge for Fe_2O_3 and Fe. At energy E_1 (E_2) Fe_2O_3 (Fe) has larger absorption, respectively, than the other component. On tomograms taken at these energies regions with different chemical state of Fe can therefore be distinguished.

becomes accessible non-destructively. The only limitation in the application of this method is the condition (eqn 17) which is setting certain limits to the values of energy and sample thickness. To meet (eqn 17) requires that there is an absorption edge not too far from the optimum energy as described above.

2.5. Resolution and Statistical Accuracy

To describe image quality in a quantitative way it is common to introduce the following parameters: (a) spatial resolution, defined by the measured modulation transfer function (MTF), and (b) statistical accuracy. Both values are needed to evaluate tomographic results properly.

Spatial resolution of any imaging device is best described in the spatial frequency domain. Spatial frequencies are expressed as lp/mm and can be thought of as a varying intensity profile of light and dark stripes. The MTF is defined in the one- or two-dimensional spatial frequency domain and there normalized to unity at zero frequency. It can be interpreted as the loss of contrast caused by the imaging system at any given spatial frequency. This description is easily extended to treat the compound imaging system by just multiplying the MTFs of the systems' components. Furthermore, the MTF analyses the detection system in detail, yielding not only the high frequency limit but also the performance at medium and low frequencies. As a parameter for fast comparison of optical systems the spatial frequency f_{10} at 10% contrast transfer is often used. The value $a_{10} = 1/(2f_{10})$ estimates the size of the smallest resolved detail. The corresponding function in the 2D spatial domain is called point spread function (PSF) and is defined as the image of a δ -shaped object point.

The measurement of MTF can be performed directly (Suzuki *et al.*, 1989) by imaging test patterns of narrow sinusoidal line profiles or indirectly (Busch, 1994) by observing a well known test object and calculating the quotient of the Fourier transforms of the image and the ideal object. Figure 11 shows MTF curves (Busch *et al.*, 1995) measured indirectly by recording a lead edge. The plots display different settings of the X-ray detector described in section 2.3.2. The best resolution in the high frequency region ($a_{10} = 2.5 \mu\text{m}$) is reached with a CdWO_4 screen at six-fold optical enlargement. The combination of the

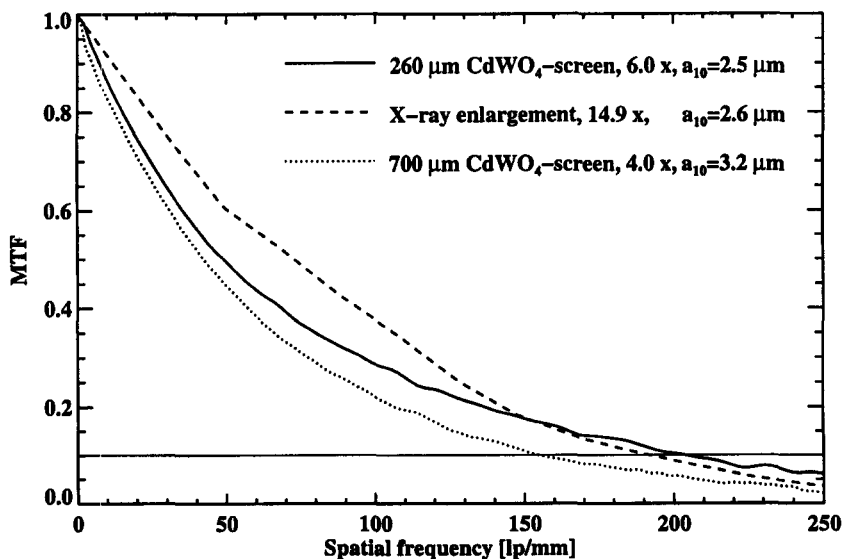


Fig. 11. Comparison of MTF curves at different detector settings, i.e. type of scintillator screen, overall magnification and whether or not X-ray enlargement is employed.

X-ray detector with X-ray enlargement yields similar resolution ($a_{10} = 2.6 \mu\text{m}$) even with a polycrystal screen but uses an overall magnification of $\times 14.9$.

Spatial resolution does not account for the accuracy of the image signal. The information contents of a given image pixel is described by the signal-to-noise ratio (SNR), defined by normalizing the image signal with respect to the statistical uncertainty. To achieve a given amount of accuracy of the CT voxel, the number of incident photons, the mean absorption of the sample, additional noise of the detector and the effect of reconstruction has to be considered. Assuming for the present an ideal detector, the noise variance of the measured absorption coefficient $\overline{\Delta\mu^2}$ in the tomogram is given by (Davis, 1994)

$$\overline{\Delta\mu^2} = \frac{\pi^2 - 3}{18w^2MN} \quad (18)$$

where w is the pixel size, M the number of projections, and N the mean number of detected photons per pixel. This relation describes the effect of reconstruction and photon statistics of the measured X-rays on the accuracy of the absorption coefficient μ .

A real detector introduces additional noise to the measured signal which is expressed by the detective quantum efficiency (DQE) introduced by R. Jones (Jones, 1959):

$$DQE := [SNR_{out}/SNR_{in}]^2 \quad (19)$$

An ideal detector has a DQE of unity, whereas real devices always decrease the SNR and therefore yield DQE smaller than one. If the DQE is known the accuracy of the tomographic system can be calculated by replacing N in eqn (18) by ($N_{\text{eff}} = N \cdot DQE$).

Typical X-ray detectors are cascaded devices employing one or more conversion steps, each of which is introducing additional noise. The variance of cascaded statistical processes is calculated by a variance theorem (Mandel, 1959) if for step i of the cascade $\bar{N}_i = \eta_i \bar{N}_{i-1}$ particles are created from the preceding step ($i-1$) then the mean variance after this step reads:

$$\overline{(\Delta N_i)^2} = \bar{\eta}_i^2 \cdot \overline{(\Delta N_{i-1})^2} + \bar{N}_{i-1} \cdot \overline{(\Delta \eta_i)^2} \quad (20)$$

where $\overline{a(\Delta N_{i-1})^2}$ is the mean variance after the preceding process, $\overline{(\Delta \eta_i)^2}$ the mean variance of the current conversion step. If the i -th process obeys Poisson statistics, $\overline{(\Delta \eta_i)^2} = \bar{\eta}_i$; this is true if $\bar{\eta}_i \gg 1$. Otherwise in the case of binomial distribution, $\overline{(\Delta \eta_i)^2} = \bar{\eta}_i(1 - \bar{\eta}_i)$; this holds for $\bar{\eta}_i \leq 1$.

This theorem (eqn 20) allows to calculate SNR for any cascaded detector by determining the variance of the whole cascade (Amemiya *et al.*, 1988; Dunsmuir *et al.*, ; Busch, 1994). Combined with eqns (19) and (20) the number of necessary photons per pixel for each projection can be estimated. If $\Delta\mu$ is the desired accuracy we have:

$$N = \frac{\pi^2 - 3}{18w^2M\overline{\Delta\mu^2} \cdot DQE} \quad (21)$$

The increase of required photons with decreasing pixel size is derived by substituting $N = F \cdot T \cdot w^2$, where F is the photon flux, and T the exposure time.

$$F \cdot T \sim \frac{1}{w^4 \cdot \overline{\Delta\mu^2} \cdot DQE} \quad (22)$$

If the required statistical accuracy and experimental condition shall remain, a linear resolution enhancement must increase by w^4 , as already mentioned above.

III. RESULTS

3.1. Point Scanning

One line of development of μ CT during the last decade was pursued by groups who already used scanning of pointbeams of conventional X-ray generators in radiography (Elliott *et al.*, 1987a; Dover *et al.*, 1988; Elliott *et al.*, 1987b, 1994a; Mummery *et al.*, 1993; Elliott *et al.*, 1990; Gao *et al.*, 1993; Anderson *et al.*, 1994; Elliott *et al.*, 1994b). Since high intensity of a pointbeam requires a source of high brilliance, microfocus X-ray tubes were usually engaged. For instance, working with characteristic Mo K α -radiation of a rotating-anode microfocus X-ray tube, a brilliance of the order of 10^9 photons/sec/mrad²/mm² contained in an energy band of $\Delta E/E = 10^{-3}$ can be achieved (Bonse, 1980). On the other hand, this is still a small brilliance when compared to that achievable with SR. For example, undulator radiation of a third-generation SR source like the ESRF surpasses the value typical for a rotating anode source by 7–8 orders of magnitude (e.g., ID 2 at the ESRF). In addition to this the SR source provides energy tuneability. Thus the advent of SR radiation made it possible to increase the spatial resolution of radiograms by using even finer pointbeams and, at the same time, to make faster measurements and hence take more data, i.e. proceed from 2D-radiography to 3D-tomography (Bowen *et al.*, 1986; Bowen, 1989).

Groups historically closer to SR used it *ab initio* to condition pointbeams for microradiography and μ CT (Borodin *et al.*, 1986; Dementyev *et al.*, 1991; Mezentsev and Pindiurin, 1987). Frequently the pointbeam-scanning apparatus is also used for micro X-ray fluorescence analysis (μ XFA) (Knor *et al.*, 1995; Dolbnya and Zolotarev, 1994). An early pointbeam-scanning experiment using photons in the range of 8 keV from a bending magnet and in the range of 16 keV from a superconducting wiggler is described in (Bowen *et al.*, 1986). Pointbeams were set up with platinum collimators measuring between 4–30 μ m in diameter. Beam-scanning was performed matching beam dimensions, i.e. in steps of 5 μ m (15 μ m) for a 4 μ m (30 μ m) beam, respectively. By the Nyquist theorem the maximum spatial resolution that can be expected for the 4- μ m aperture and 5- μ m steps is 2–2.5 μ m. Due to air scatter, scatter by collimator edges, by the specimen itself etc., the resolution practically achieved was certainly worse. Nevertheless, using the principle of this technique, tomograms of remarkable detail were taken of a number of samples of interest to medicine or biology including sections of human femur (Bowen *et al.*, 1986) and iliac (Elliott *et al.*, 1994a) bone, human teeth under acid attack and the remineralization of subsurface enamel solutions (Elliott *et al.*, 1994a; Gao *et al.*, 1993), human lymph node (Borodin *et al.*, 1986) or the smashing limb from a mantid shrimp (Elliott *et al.*, 1994a).

The collimation of microbeams is usually achieved with the help of pinholes which then limit the spatial resolution to about half their diameter, i.e. to > 1 μ m. However, as McNulty *et al.* (McNulty *et al.*, 1995; Haddad *et al.*, 1994) have shown, by using a phase-zone plate of nickel for focusing and SR from an undulator at $\lambda = 3.6$ nm wavelength, a sub-micrometer focal spot of about 73 nm diameter at the specimen can be obtained. Scanning with this spot a test sample consisting of gold lines 100–300 nm in width, the spatial resolution in the reconstructed 3D image was found to be close to 73 nm. In a similar fashion, in order to reduce the size and increase the intensity of a pointbeam at a conventional X-ray tube, Gurker *et al.* (Gurker *et al.*, 1994) used a multilayer mirror for focusing the beam down to a horizontal spot size of 18 μ m in the specimen. As seen in Fig. 12 the geometry of focusing implies that behind the specimen the beam widens again which permits to use a detector with somewhat lower spatial resolution. This is an additional advantage over simply using the unfocused pointbeam. Samples investigated by this method include the head and abdominal section of a bumble bee, a cherry stone, and pieces of balsa and pine wood. The method was also used for fluorescence point-scanning and then compared with the information obtainable by employing line-scanning fluorescence imaging at a SR source (Bavdaz and Gurker, 1993). The point-scanning method was found to yield a better signal-to-noise ratio.

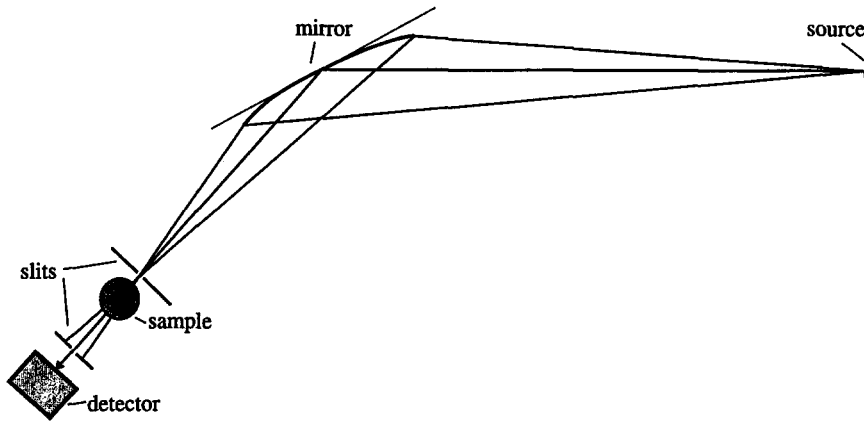


Fig. 12. Point focusing with mirror (after Gurker *et al.*, 1994).

3.2. Line Scanning

With a pointbeam, in order to measure a sample volume, one has to scan the three independent variables x , φ , and z which is quite time consuming. On the other hand, by using a ribbon-shaped line beam in combination with a multi-element line detector like a photodiode array, the x-scan is replaced by simultaneous exposure and the scan time can be reduced by a factor of 100–1000. The experimental set-up for line-scan tomography at HASYLAB (Engelke *et al.*, 1989a) is shown in Fig. 13. At a distance of 30 m from the X-ray wiggler the horizontal extension of the linebeam is wide enough to investigate samples with slice diameters of 50 mm. In the original design, in order to fully cover 50 mm two photodiode arrays in line, each 25 mm long, are employed. The incident beam is monochromatized by a channel-cut crystal in front of the sample. X-Rays are converted

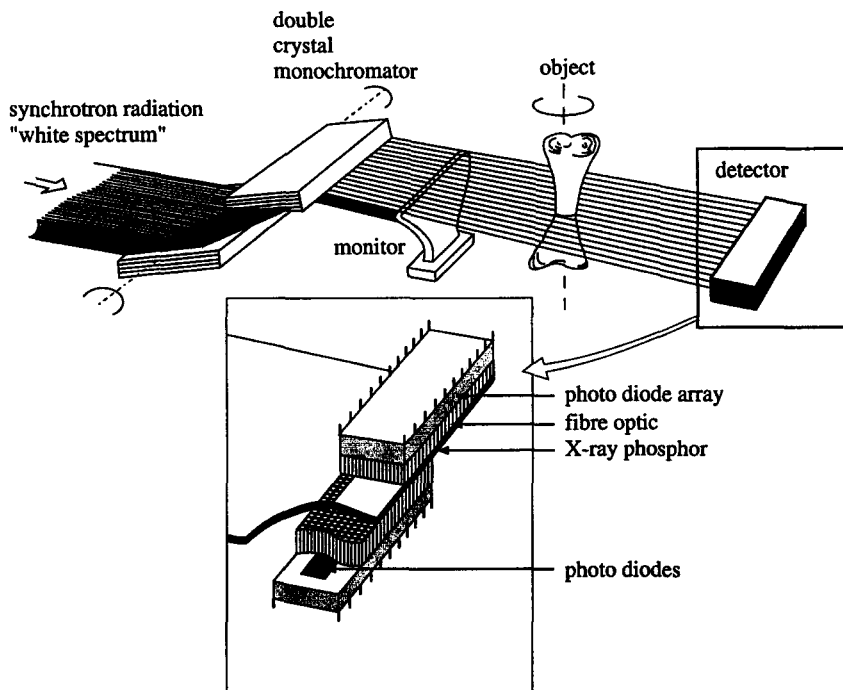


Fig. 13. The experimental set-up for line-scan tomography at HASYLAB (after Engelke *et al.*, 1989a).

to light by means of a scintillator screen combined with a fibre optic consisting of 6- μ m circular fibres directly in contact with the diode arrays which have 25 μ m pitch. A third photo-array detector is monitoring the monochromatic beam incident on the sample. Spatial resolution is limited by light diffusion in the phosphor layer ($\text{Gd}_2\text{O}_2\text{S:Tb}$) of the screen to about 50 μ m.

Using this system Engelke *et al.* (Engelke *et al.*, 1989b) analysed the calcium distribution in a human finger bone. In order to discriminate the bone material from non-calcified tissue they employed a technique known as dual energy contrast which is based on the fact that the energy dependence of the Compton- and photon-absorption cross-sections is remarkably different for materials of different Z . By measuring at two different energies, e.g., 37 keV and 20 keV, Engelke *et al.* could separate regions with Ca and P (higher Z) from regions with H_2O and C (lower Z). They calibrated the method with the help of tomograms of phantom samples containing $\text{K}_2\text{HPO}_4 \cdot 3\text{H}_2\text{O}$ solutions of known concentration. Thus a quantitative determination of the Ca-distribution is possible provided the sample can be assumed to be a two-component system which for bone is a good approximation. The advantage of the dual energy method over working directly at the Ca K-edge (4.03 keV) is that, because of too much absorption at 4.03 keV, the latter procedure is impracticable for samples with thickness above a few millimetres. Comparing the CT technique (Engelke *et al.*, 1993) to microradiography and histologic sectioning it was found that the CT technique requires almost no sample preparation. To obtain high resolution the use of SR is necessary. A slightly different system (Nagata *et al.*, 1992) in which radiation from a vertical wiggler and a double crystal monochromator *behind* the sample was used in combination with a photodiode array detector, the structure of sintered iron ore was studied.

For materials with higher Z , the possibilities for identifying different materials as function of the spectrum was studied in more detail using defined phantom samples (Suzuki *et al.*, 1988; Hirano *et al.*, 1989a; Suzuki *et al.*, 1990).

3.3. Cone Projection and Fan Scanning

Non-parallel beam geometries are best adapted to the use of microfocus X-ray tubes and cannot profitably be operated with SR. Nevertheless we like to describe results obtained by these techniques, mainly because the development of μ CT was pushed to a considerable extent by groups (Feldkamp *et al.*, 1989) working initially with medical CT scanners where fan geometry is the normal case. Furthermore, in the context of the present review, a comparison of the scopes and capabilities of conebeam μ CT and SR μ CT appears to be very useful.

A decisive step in establishing conebeam μ CT was the construction of an operable conebeam algorithm by Feldkamp *et al.* (Feldkamp *et al.*, 1984). A typical conebeam apparatus is described in Feldkamp *et al.*, 1989. As X-ray source, a 5- μ m microfocus tube operated at 60 kV and 5–100 μ A current with 500- μ m Be filter is employed. Full-cone data acquisition is achieved by using as 2D-detector an image intensifier in combination with a vidicon camera and a digitizer. A 3D-projection data set consists of 129 angular settings including a sum of 200 eight-bit video frames at each position with 250×200 pixels of 40- μ m spacing each. Raw data were corrected by taking background and reference images with the sample removed from the beam. The technique is applied to the study of the 3D-structure of human cancellous bone *in vitro* (Feldkamp *et al.*, 1989; Kuhn *et al.*, 1990). The reconstructed region of a standard bone cube was $8 \times 8 \times 6$ mm. Reconstruction points were 50 μ m apart. A typical reconstruction set contained $200 \times 200 \times 120$ points. For reconstructed data the spatial resolution is approximately 70 μ m. The analysis of the 3D structure included: threshold determination, computation of structural indices (Parfitt *et al.*, 1987) like BV/TV, BS/BV (BV bone volume, TV total volume, BS bone surface), Tb.Th (trabecular thickness), Tb.N (trabecular number), Tb.Sp (trabecular separation), connectivity, and structural anisotropy. A wide range of different types of structural architecture was revealed, varying in particular with the region in the body from where the autopsies had been taken. The 3D information was compared to

that obtainable by 2D histological sectioning and found to be superior in that a better qualitative understanding of the complex 3D structure of trabecular bone is achieved. However, upon regarding the results in more detail, systematic structural differences between 3D and 2D observation became quite evident. Discrepancies were attributed to insufficient spatial resolution of the applied kind of conebeam tomography. With the same tomographic scanner femurs of guinea pigs after myectomy were examined in order to study architectural changes subchondral bone might be undergoing in the early stages of osteoarthritis (Layton *et al.*, 1988; Dedrick *et al.*, 1991). Similarly, more recent studies (Goulet *et al.*, 1994; Goldstein *et al.*, 1993) were devoted to establish a relationship between the 3D architecture of trabecular bones as observed by cone beam μ CT and their mechanical integrity. Furthermore, in order to find out about the influence of the production of oestrogen on the structural and mechanical properties of bone an investigation of retired breeder beagles after ovariectomy was performed (Goldstein *et al.*, 1993). Although in general the results look promising it is clear that many more investigations will be necessary before generally valid conclusions can be drawn. In particular, as much as the technique of μ CT is concerned, it appears that eliminating beam-hardening effects (e.g., by using a monochromatic source), improving the spatial resolution, and increasing the pixels' information depths (linearity) would be valuable to this end.

As was demonstrated recently (Castelli *et al.*, 1994; R  gsegger *et al.*, 1996), by bringing the scintillation layer closer to the CCD, the detector's quantum efficiency can be increased considerably. Fast measurements become possible even when using a standard microfocus X-ray tube with 10 μ m spot size, operated at 100 μ A, a mean energy of 30 keV with 50 keV peak value. For measuring a single slice of 20–30 μ m thickness and a maximum diameter of 17 mm, 1–2 min exposure time is needed. A sample 20–30 mm high is then measured in less than 1 hr. The system is applied to the study of trabecular bone structure. However, placing the scintillator screen in direct contact to the CCD reduces the spatial resolution at least by a factor of two. At nominal resolution (CCD pixel size) of 8–14 μ m the resolution deteriorates to 20–28 μ m. As we shall discuss below, similar speed without impairing spatial resolution can be attained probably only by improving the detector further or by using SR and parallel beam geometry.

Conebeam microtomography using the microfocus source inside a SEM (Thomas *et al.*, 1992; Fuhrmann, 1993) as described above and a cooled CCD as 2D detector included specimens like an electronic Si-diode and a small sea shell (Cazaux *et al.*, 1994). Since the target material and hence the X-ray spectrum can easily be changed the method is well adapted to investigate variations of elemental concentration in the sample by subtraction contrast (Cazaux, 1993; Sasov and Cazaux, 1994).

3.4. Parallel Projection

A typical μ CT camera for parallel projection, developed at the University of Dortmund, is shown in Fig. 14. It follows earlier designs (Bonse *et al.*, 1986; Johnson *et al.*, 1986; Bonse *et al.*, 1989) and incorporates the CCD-based 2D detector for X-rays of Fig. 5 (Busch *et al.*, 1995). The incident beam is monochromatized by a standard double-crystal monochromator for use at a high intensity SR source which can be a bending magnet or, preferably, a multipole wiggler like BW2 at DORIS/HASYLAB, Hamburg, or ID11 at the ESRF, Grenoble. The content of harmonics is reduced by operating on the flank of the rocking curve of the monochromator. Suppression of harmonics works better the more efficiently the first crystal is cooled to avoid its bending under the heat load of the direct beam from the storage ring. Some SR beamlines are additionally equipped with a pair of mirrors for even better cut-off of higher harmonics, for reducing the heat load, and/or for focusing of the beam. While beam focusing is counter-acting parallel projection, the increased rejection of harmonics and reduction of heat load is often quite useful, especially at high power beamlines where it is difficult to avoid thermal bending of the first crystal completely.

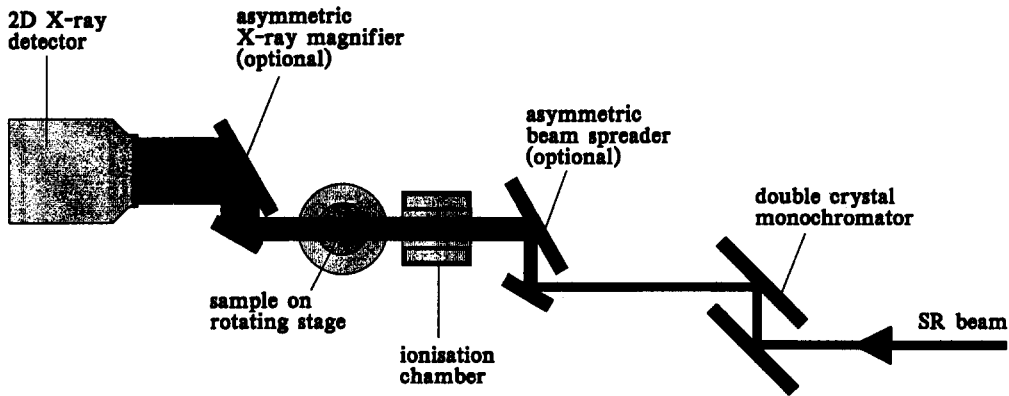


Fig. 14. Tomographic camera with 2D-parallel projection geometry, to be used at any standard SR beamline with double-crystal monochromator (Bonse *et al.*, 1991).

The beam incident on the sample should be wide enough both in x- and in z-direction (Fig. 1) to accommodate larger specimens and at the same time be homogeneous to minimize the need for intensity normalization. Because of the strong collimation of the SR beam on the order of 0.1 mrad the beam size as delivered by the source is not always sufficient. At present SR sources monochromators are 30–50 m away from the electron orbit. Assuming the electron beam to be 0.15 mm (1.3 mm) high at the ESRF (at DORIS III) we calculate maximum specimen heights of about 3.15–5.15 mm (4.3–6.3 mm), respectively. In cases where this is not enough an asymmetrically reflecting beam spreader, either mono- or polythitic, is used (Bonse *et al.*, 1986). At SR laboratories where the tomography user can devise the monochromator to already widen the beam no separate beam spreader is needed. An example for this is shown in Fig. 15 (Takeda *et al.*, 1994). As far as homogeneity of the beam is concerned, the use of mirrors is not unproblematic since with mirrors the intensity distribution over the beam cross-section usually becomes less homogeneous. Similarly, at SR sources with extreme small source size, i.e. because of too coherent illumination, speckle patterns due to unavoidable beryllium windows somewhere upstream in the beamline also affect the homogeneity of the intensity distribution.

The sample is mounted on a precision rotary stage which is not only capable of angular increments well below 0.1° per motor step but also has a provision to withdraw the specimen from the beam when a reference image is taken and place it back to the same

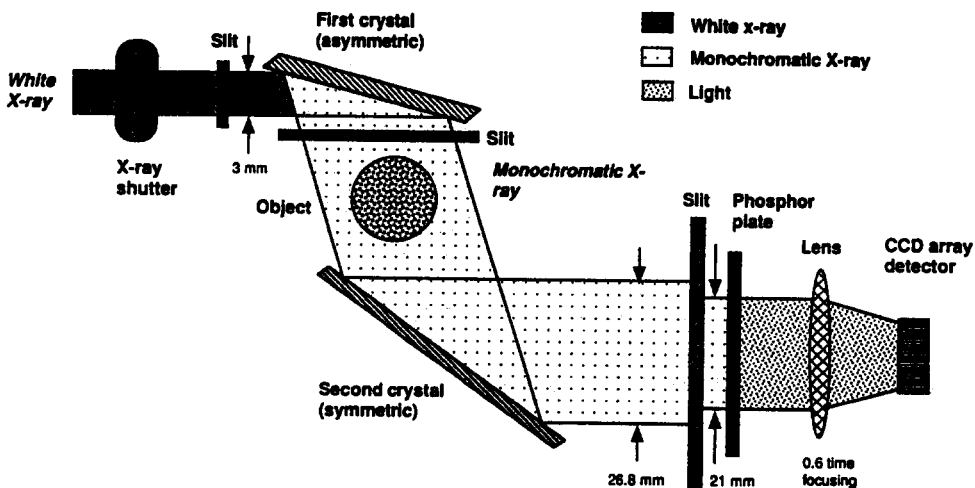


Fig. 15. SR beamline where the adaption of beam width to the sample size is accomplished inside the double-crystal monochromator of the beamline (after Takeda *et al.*, 1994).

position very accurately afterwards. Behind the sample the X-ray magnifier described in section 2.3 can be employed. With energies varying from 7.7–11.3 keV X-ray magnifications from about two- to tenfold (Nußhardt, 1990; Bonse *et al.*, 1991) are achieved. Variations of this system consist mainly in employing different 2D-detectors, e.g., a X-ray sensing pickup tube (Suzuki *et al.*, 1989; Tanak *et al.*, 1993; Masuda *et al.*, 1990; Hirano *et al.*, 1990; Hirano and Usami, 1989; Hirano *et al.*, 1989b, 1995) or a lithographically fabricated cellular phosphor plate imaged to the CCD (Flannery *et al.*, 1991; Dunsmuir *et al.*, 1991; Deckman *et al.*, 1989).

A number of groups have successfully applied parallel-projection μ CT to problems in materials science. Absorption-edge differencing is used to separately identify elements adjacent in the periodic table (Bonse *et al.*, 1986; Kinney *et al.*, 1986a; Johnson *et al.*, 1986; Kinney *et al.*, 1986b; Bonse *et al.*, 1989, 1992; Nußhardt *et al.*, 1991) or even the same element in different chemical states (Kinney *et al.*, 1986a; Johnson *et al.*, 1986; Kinney *et al.*, 1986b). For materials which contain either too many different elements or low-Z and high-Z elements at the same time, absorption-edge differencing is less suited because average absorption may be too high to work at the edges of the light-element components. Examples of this are meteorites (Hirano *et al.*, 1989b, 1990) containing various different elements in the range from Si to Ni. The authors could show that, in situations like this, working at 30 keV, i.e. above all K-edges concerned, and calibrating the system with the help of phantoms of known composition, the fairly complicated composition of meteorites could be determined. Objects frequently studied include metal-matrix (Stock *et al.*, 1989; Kinney *et al.*, 1989; Bonse *et al.*, 1991; Kinney and Nichols, 1992; Kinney *et al.*, 1991b; Bonse *et al.*, 1992; Zywiec *et al.*, 1993; Kinney *et al.*, 1991a), ceramic-matrix (Kinney and Nichols, 1992; Kinney *et al.*, 1993, 1994b), and epoxy-matrix composites (Nußhardt *et al.*, 1991). Provided the fibres have a density sufficiently different from that of the matrix, e.g., SiC fibres in Al, individual fibres only a few micrometers thick can be seen in the 3D image (Kinney *et al.*, 1991b; Stock *et al.*, 1989; Hirano and Usami, 1989). Similarly, alloy precipitates, e.g., Mg_2Si in Al, only 5 μm in size were identified in tomograms. Matters of interest that were studied included the process of vapour infiltration of the ceramic matrix into the meshes of the 2- or even 3D preform, i.e. the structure built of fibre cloth to be then vapour-infiltrated (Kinney *et al.*, 1993, b), the fibre reaction under tensile stress in metal-matrix composites (Kinney *et al.*, 1991a; Zywiec *et al.*, 1993; Tanak *et al.*, 1993; Hirano *et al.*, 1995), the ductile rupture of Al foil between sapphire blocks (King *et al.*, 1995), and small catalyst particles of Pd supported in carbon foam (Nichols *et al.*, 1989). Another group investigated coal, sandstone and the porosity in an unsintered bead pack (Flannery *et al.*, 1987; Dunsmuir *et al.*, 1991). There are also studies to directly verify whether certain small-scale structures are truly imaged on tomograms. Examples are the tomogram of a laser fusion microballoon known to have a wall consisting of an 8- μm glass layer coated with 32 μm of plastic (Kinney *et al.*, 1988), alloy-phase precipitates of sizes near 15 μm that could also be seen and accurately measured (Bonse *et al.*, 1991) on back-scattered electron-micrographs (BSE), and blood-vessel canals in human trabecular bone which are seen both in the tomogram and the histologic section prepared of the same location in the specimen (Bonse *et al.*, 1994).

Parallel projection μ CT is very well suited to investigate bone structures. Figure 16 shows the trabecular structure of human iliac crest which we measured at beamline BW2 at DORIS/HASYLAB using the tomographic camera of Fig. 14. In an investigation (Bonse *et al.*, 1994, 1996a,b) performed jointly with Prof. G. Delling, Division of Osteopathology, University of Hamburg, a series of biopsies were selected from patients suffering from various bone diseases. The two pictures in Fig. 16 illustrate the loss of mineralized bone substance with progressing osteoporosis as a result of long-term haemodialysis. Figure 17 shows the formation of so-called microcallus structure (Delling *et al.*, 1995), which is tentatively interpreted as the formation of new bone after the occurrence of bone microfracture. Kinney *et al.* applied parallel μ CT (Kinney *et al.*, 1994a; Majumdar *et al.*, 1996) to image the trabecular bone structure of rat proximal tibias *in vivo* in order to investigate the influence of oestrogen depletion induced by

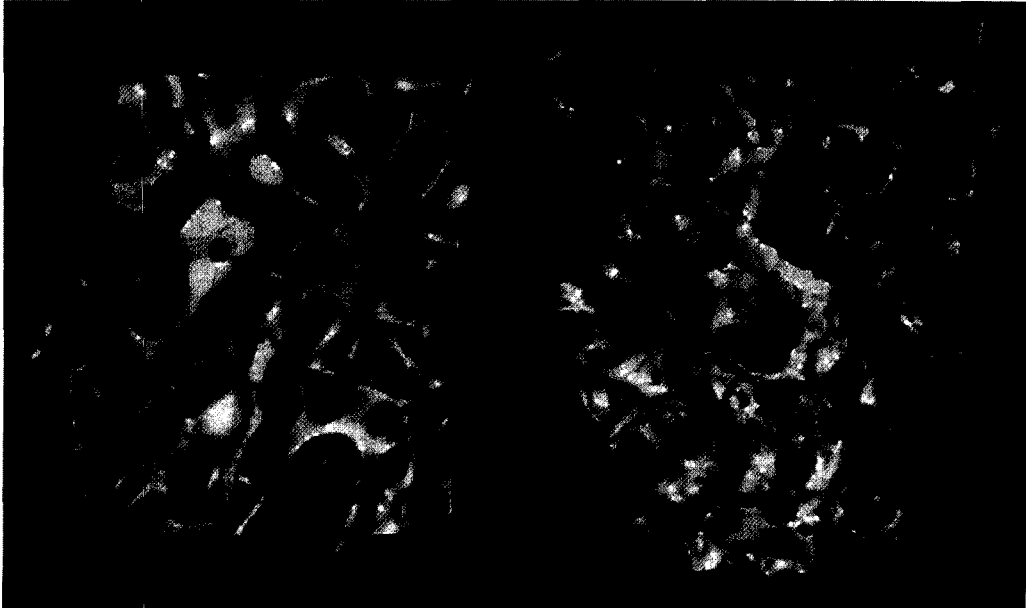


Fig. 16. μ CT images of trabecular structure of human iliac. At the right the loss of mineralized bone substance with progressing osteoporosis is evident.



Fig. 17. μ CT images of human trabecular bone samples with microcallus formation.

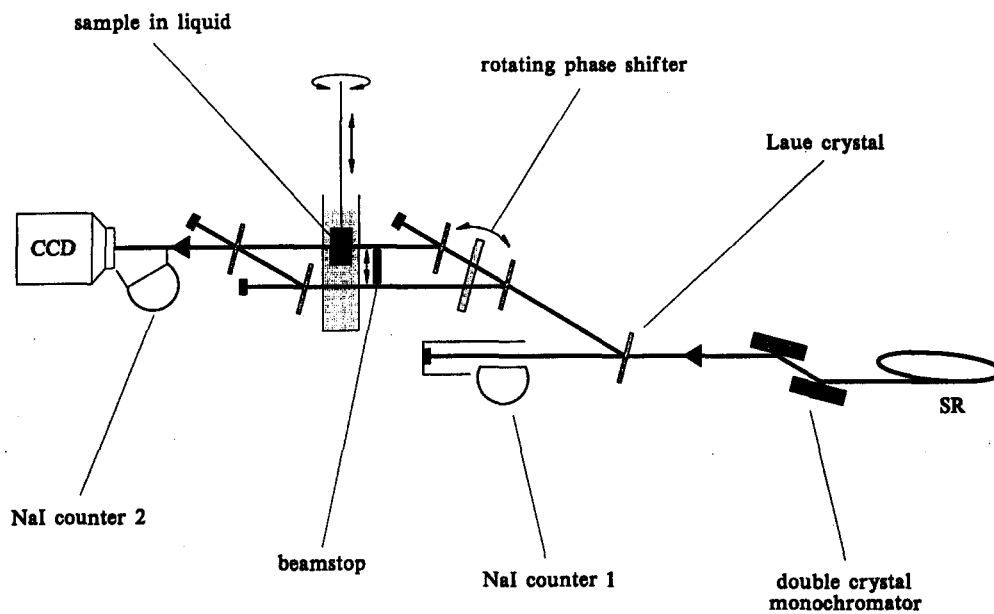


Fig. 18. Schematic view of camera for X-ray phase-contrast μ CT.



Fig. 19. Phase-contrast tomogram of a rat cerebrum. Different 3D views show internal structure. Details like white and grey matter can be seen.

ovariectomy. The ovariectomized rats lost 65% of their trabecular bone volume as compared to an insignificant change in the non-ovariectomized rats (Kinney *et al.*, 1995b; Lane *et al.*, 1995). Similarly the μ CT method was used, in combination with atomic force microscopy, to study the stability of fully hydrated coronal dentine of third molars as it undergoes demineralization (Kinney and Nichols, 1992; Kinney *et al.*, 1995a, 1996a,b,c). There are also impressive examples of μ CT imaging applied to 3D visualization of anatomical details in small animals like the head of a live rat (Takeda *et al.*, 1994) or of a caterpillar (Ando and Hosoya, 1972).

The quantitative investigation of bone structure with structural parameters (Parfitt *et al.*, 1987) as described in section 3.3 for conebeam projection is with parallel-projection μ CT also well possible. However, we expect that parallel-projection μ CT, when performed at the present state of the art, yields the more reliable structural information. This seems to apply to positional accuracy, to resolution and, even more, to the measured μ -density distribution throughout the sample volume. The major reason is that conebeam projection normally has to use polychromatic radiation and is therefore more apt to become affected by beam-hardening. On the other hand, the advantage of conebeam μ CT not to need SR and yet be about equally fast, certainly weighs very much.

3.5. Phase-contrast μ CT

As already pointed out at the beginning of section 2.4 above, because of the different dependence on atomic number Z , phase contrast is very much larger than absorption contrast for substances consisting chiefly of light elements. Therefore, phase-contrast μ CT is expected to be principally better suited for imaging organic matter than is absorption-contrast μ CT, where the (silent) assumption is that efficient methods to record and image phase shifts also exist in the X-ray range.

The best and most direct way to measure X-ray phase-contrast is with the X-ray interferometer (Bonse and Hart, 1965a). The first phase-contrast radiograph was that of a plano-concave epoxy plate recorded with the asymmetric triple Laue-case (LLL) interferometer some time ago (Bonse and Hart, 1965b). Ando and Hosoya (1972) were able to image cortical bone tissue of a human femur by X-ray phase-contrast. With the neutron interferometer phase-contrast radiographs of magnetic domain structures were studied (Schlenker *et al.*, 1980).

Another possibility to record X-ray phase effects of an object are projection micrographs taken inside a double diffractometer (Takeda *et al.*, 1994), or with highly coherent undulator-SR (Snigirev *et al.*, 1995). It appears that contrast contours seen with coherent SR are primarily effects of the gradient dn/dr of the refractive index n and not so much caused directly by n . This makes the reconstruction of coherent-SR projections more complex and the interpretation of structures in 3D presumably more difficult than it is with the interferometric measurement of n .

Recently, by using the LLL interferometer, the first 3D X-ray phase-contrast images could be made. Objects imaged include a plastic sphere with bubbles (Momose, 1995; Momose *et al.*, 1996), part of a rat cerebellum and of a cancerous rabbit liver (Momose and Fukuda, 1995; Momose *et al.*, 1995, 1996), and a mouse kidney (Beckmann *et al.*, 1995).

Figure 18 shows the set-up used by us at DORIS/HASYLAB for X-ray phase-contrast μ CT (Beckmann *et al.*, 1995, 1996). Evidently, by working with a skewsymmetric interferometer much specimen space is provided in the interfering beams. The sample is inside a liquid cell extending over both beams. Using a rotating phase-shifter N interferometric projections are taken at phase positions $2\pi l/N$ ($l=0,1,\dots,N-1$). For accurate normalization of projected intensities, reference images with the sample withdrawn from the beam are recorded in between. The number of references needed depends strongly on SR-source stability and effective shielding of the interferometer against thermal and vibrational disturbances. The additional Laue fore crystal was found not to be necessary in a slightly modified camera employed later at the ESRF (Beckmann *et al.*, 1996). Since a phase signal is periodic in 2π a special algorithm was developed

(Beckmann, 1997) to free the measured projection data from their 2π ambiguity. Figure 19 shows the tomogram of a rat cerebrum; the sample was provided by the Institute of Cell Biology (IFZ), Essen, Germany. Various structures of interest like white and grey matter are visible. It was found that with these low- Z specimens the visibility of details is almost entirely due to phase-contrast, and practically no contours are seen on absorption-contrast tomograms of the same sample regions. From this the new possibilities of phase-contrast X-ray tomography become apparent. At the same time situations can be foreseen where the combination of both kinds of contrast will be useful. An example would be the investigation of some medium- or high- Z object embedded in organic matter, e.g., an implant, a sensor or similar, where the heavier component would be studied by absorption-edge differencing.

In the following we want to compare phase- and absorption-contrast μ CT in a quantitative manner. In the first step we examine the difference between either type of contrast for light- and medium- Z elements as a function of photon energy E . The second step is to compare the phase-contrast of different low- Z substances with varying E .

Let us assume that in projections 1% intensity change is detectable which is not difficult when a CCD detector featuring a typical 5×10^3 – 10^4 dynamic range is used. We further suppose that optimum specimen thickness t has been chosen, which means $\mu t = 2$ for absorption contrast and $\mu t \ll 1$ for phase-contrast. The latter condition ensures that the contrast of interference-fringes is practically not affected by absorption. If thicker specimens have to be investigated one can compensate amplitude reduction of the beam which runs through the specimen by placing a parallel plate of matching absorption in the other inferring beam. A compensating plate should also be used for limiting the maximum interference order m to $m < E/\Delta E$ where $\Delta E/E$ is the relative bandwidth of the radiation used. Otherwise the interference contrast is spoiled by dispersion effects in the specimen.

We now calculate $t_{1\%}$, (1% thickness) defined as the increment in specimen thickness causing 1% change of the detected signal under the conditions specified above. With this definition, high detection sensitivity of a material is equivalent to a small $t_{1\%}$ value and vice versa.

In the case of absorption we write the intensity signal I_{ab} behind the specimen as

$$I_{ab} = I_0 \exp(-\mu t) \quad (23)$$

I_0 is the incident intensity. Using $\mu t = 2$ and the base $e = 2.7183$ of the natural logarithm we find

$$t_{1\%ab} = e^2/(100\mu) \equiv 0.0739/\mu \quad (24)$$

The phase-contrast intensity signal I_{if} behind the interferometer varies sinusously with thickness t and can be written as

$$I_{if} = \{1 + (1 - b/2)\cos(2\pi t/200t_{1\%}) + b/2\}/2 \quad (25)$$

The factor $1/2$ normalizes I_{if} to 1. b is the background and related to the fringe contrast γ by

$$b = 2(1 - \gamma)/(1 + \gamma) \quad (26)$$

Monotonous sections of I_{if} have maximum length π , and implicitly in eqn (25) we have defined $t_{1\%}$ as

$$t_{1\%ph} \equiv t_{\lambda}/200 \quad (27)$$

where $t_{\lambda} \equiv \lambda/(1 - n)$ is the material thickness causing a phase shift of 2π . We further define an "advantage factor" AF of phase-contrast over absorption-contrast as

$$AF \equiv t_{1\%ab}/t_{1\%ph} \quad (28)$$

AF is large when phase-contrast gives a larger signal change than absorption-contrast.

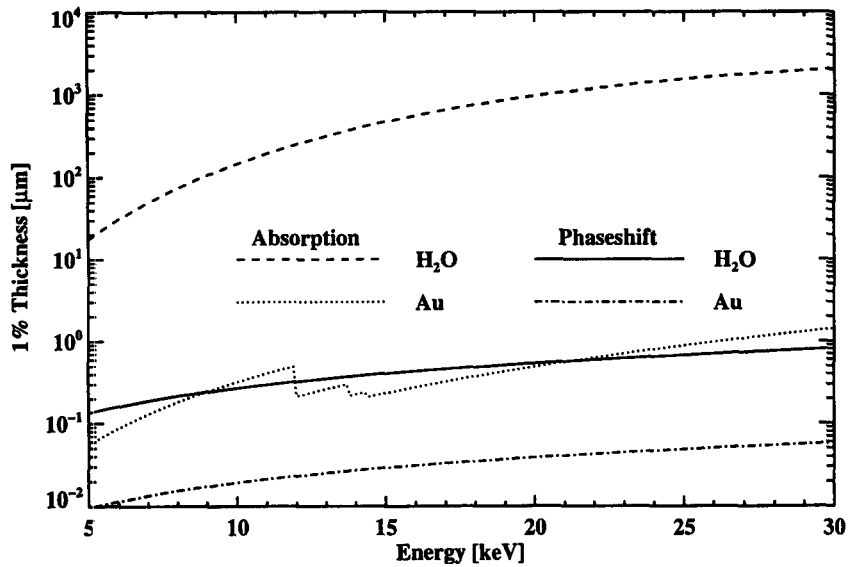


Fig. 20. Z-dependence of $t_{1\% \text{ ab}}$ and $t_{1\% \text{ ph}}$ for the low-Z material water and the high-Z material gold in the energy range from 5 to 30 keV. $t_{1\% \text{ ab}}$ and $t_{1\% \text{ ph}}$ are material thickness for 1% signal change in the case of absorption and phase tomography, respectively. Note that $t_{1\% \text{ ph}}$ is always smaller than $t_{1\% \text{ ab}}$, however much less so for gold than for water.

Figure 20 shows the Z-dependence of $t_{1\% \text{ ab}}$ and $t_{1\% \text{ ph}}$ for the low-Z material water and the high-Z material gold in the energy range from 5 to 30 keV. As expected AF is roughly two orders of magnitude larger for water than for gold. Furthermore, even for gold $AF \approx 10$ which means that also high-Z materials would give better contrast with phase than with absorption μ CT.

In Fig. 21 we show $t_{1\% \text{ ph}}$ as function of photon energy for a selection of light materials. Differences are mainly caused by differences in density ρ . Multiplying $t_{1\% \text{ ph}}$ with ρ normalizes the phase effect to the amount of mass M needed per beam area A for 1% signal change

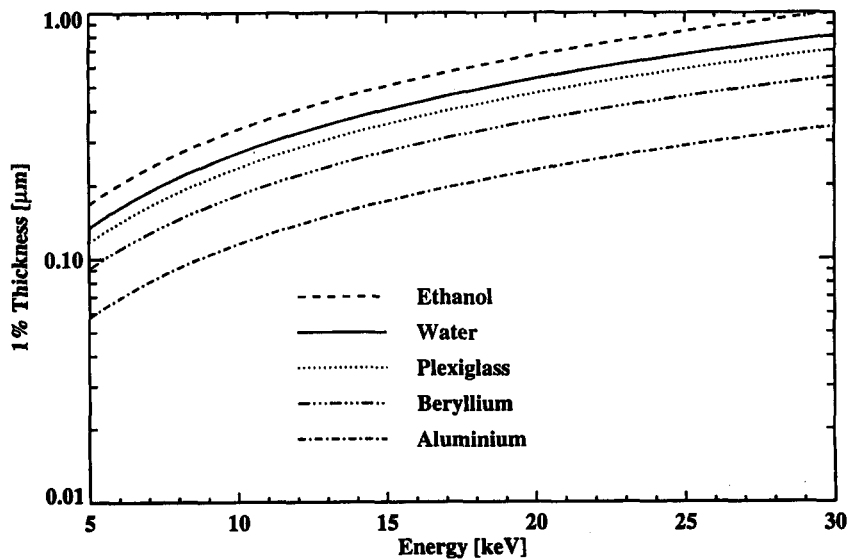


Fig. 21. 1% thickness for selected low-Z materials in phase-contrast. Differences are mainly due to different densities ρ .

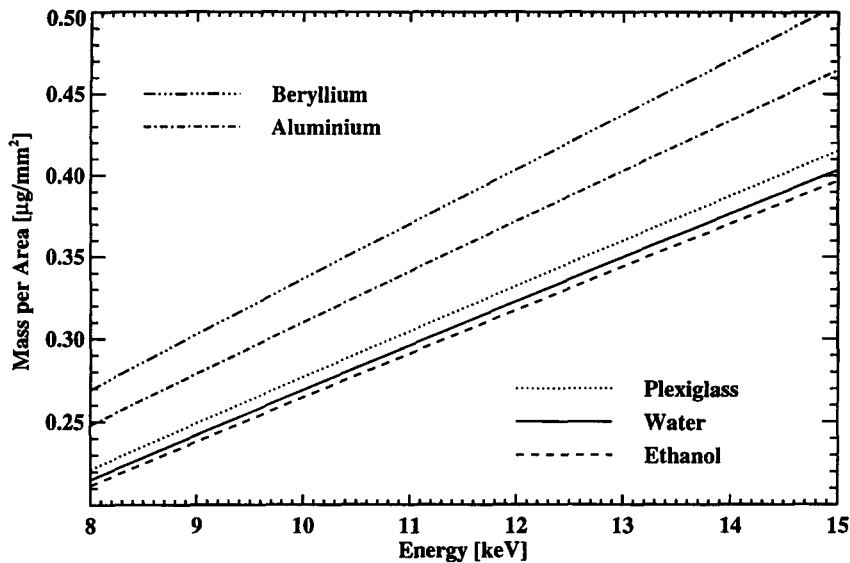


Fig. 22. Mass per beam area needed for 1% signal change for selected low-Z materials. Note that substances which contain relatively more hydrogen (Ethanol, water) yield more phase contrast than others (Plexiglass, Be, Al).

$$M \equiv \rho t_{1\%ph} \quad (29)$$

M is shown in Fig. 22 for the same materials as in Fig. 21. As is seen substances which contain relatively more hydrogen like ethanol and water yield more phase-contrast. The reason is that hydrogen contributes about twice as much charge per mass than all other elements. Therefore phase-contrast is more sensitive to hydrogen than to other elements, a property already known from and exploited in NMR tomography. It seems that the increased sensitivity to hydrogen could be the basis of phase-contrast μ CT to be specifically sensitive with respect to different organic tissues.

IV. OUTLOOK

There is already a variety of valuable examples where microtomography using SR has proven to be a useful tool in biology and medicine. At the same time it is apparent that in most of those cases either the improvement of the results or the possible application to other quite similar problems is desirable and feasible. Many more applications are expected in the future.

Microtomography has been developed by a large number of different groups and through a number of different methodical approaches. No doubt SR has kindled this development, although in parallel also new ideas and possibilities came up to improve techniques tailored to X-ray tube sources. One may wonder if methods operable at and typical for use with a conventional source will become less important. The answer is probably no.

One reason seems to be that a great advance in the development of area detectors for X-rays is just about to occur. The quantum efficiency is increased by a factor of 10–100 when the scintillator is brought very close to the CCD instead of imaging the light image on the scintillator to the CCD by an optical lens. Simply covering the CCD with a scintillator layer would spoil the spatial resolution by light diffusion in the screen and direct cross talk between neighbouring CCD pixels. Furthermore radiation damage of the CCD has to be avoided. A first step to regain resolution at least in part is to use a fibre optic between scintillator and area CCD (Castelli *et al.*, 1994) or the linear CCD (Rüegsegger *et al.*, 1996). A certain disadvantage is that additional light reflecting surfaces

are introduced and also that moiré artefacts can occur between fibre-optical plate and the lattice of CCD pixels. The best solution seems to be to fit each CCD pixel directly with an individual scintillator cell of equal size and sufficient thickness for giving high efficiency and providing radiation protection. Employing modern methods of micro-fabrication this should be possible to accomplish, including establishing cross-talk shielding between neighbouring scintillator cells and maintaining both high spatial resolution and dynamic range. Making exposures 10–100 times faster with no compensating disadvantage frees tomographic techniques using X-ray sources like conebeam microtomography from being extremely time consuming. Therefore, the application of the conebeam method to bone structure investigation and other related studies is likely to become widely-spread.

On the other hand, the number of high-power high-quality SR sources and their availability is increasing world-wide. In our context, the strength of SR and superiority over conventional sources, namely tuneability and high brilliance will be at hand to many more researchers who understand the value and make use of it. Generally speaking, the outstanding properties of SR make it the better choice when chemical identification, high spatial resolution and strict avoidance of beam-hardening errors are the main issue. Furthermore, with considerably faster measurements becoming possible spatial resolution well below 1 μ m and studies of dynamic processes in 3D should be feasible when using SR.

ACKNOWLEDGEMENTS

Our thanks are due to W. Graeff at HASYLAB/DESY, Hamburg, and to our colleagues O. Günnewig, F. Beckmann, H. Uebbing, Th. Biermann, M. Nußhardt, and M. Bartscher, University of Dortmund, for fruitful discussions on various topics related to this review. We would also like to thank the Bundesminister for Bildung und Forschung, BMBF, for financial support under contract No. 05 SPEAAB1.

REFERENCES

- Amemiya, Y., Matsushita, T., Nakagawa, A. and Satow, Y. (1988) Design and performance of an imaging plate system for X-ray diffraction study. *Nucl. Instrum. Meth. Phys. Res. A* **266**, 645–653.
- Anderson, P., Davis, G. R. and Elliott, J. C. (1994) *Microtomography, Microscopy and Analysis*, pp. 31–33.
- Ando, M. and Hosoya, S. (1972) An attempt at X-ray phase contrast microscopy. In *Proceedings of the Sixth Int. Conf. On X-Ray Optics and Microanalysis*, pp. 63–68 (eds. G. Shinoda, K. Kohra and T. Ichinokawa), University of Tokyo Press.
- Bavdaz, M. and Gurker, N. (1993) Coded imaging X-ray microprobe. *X-Ray Spectrom.* **22**, 65–70.
- Beckmann, F. (1993) *Untersuchung der Möglichkeiten der Mikrotomographie an konventionellen Röntgenquellen*, Diplom. thesis, Univ. Dortmund, Germany.
- Beckmann, F. (1996) *Entwicklung und Aufbau einer optimierten Methode der Röntgenphasenkontrast-Mikrotomographie*, PhD thesis, Univ. Dortmund, Germany.
- Beckmann, F., Bonse, U., Busch, F., Günnewig, O. and Biermann, T. (1995) A novel system for X-ray phase-contrast microtomography. *HASYLAB Jahresbericht 1995*, 691–692.
- Beckmann, F., Bonse, U., Busch, F. and Günnewig, O. (1996) X-ray microtomography (μ CT) using phase-contrast for the investigation of organic matter. *J. Comput. Assist. Tomogr.* (in preparation).
- Bonse, U. and Hart, M. (1965a) An X-ray interferometer. *Appl. Phys. Lett.* **6**, 155–156.
- Bonse, U. and Hart, M. (1965b) An X-ray interferometer with long separated interfering beam paths. *Appl. Phys. Lett.* **7**, 99–100.
- Bonse, U. (1980) X-ray sources. In *Proceedings of Nato Advanced Study Institute, Durham, England, on Characterization of Crystal Growth Defects by X-ray Methods*, pp. 298–319, Plenum.
- Bonse, U., Busch, F., Günnewig, O., Beckmann, F., Pahl, R., Delling, G., Hahn, M. and Graeff, W. (1994) 3D computed X-ray tomography of human cancellous bone at 8 μ m spatial and 10^{-4} energy resolution. *Bone and Mineral* **25**, 25–38.
- Bonse, U., Busch, F., Günnewig, O., Beckmann, F., Delling, G., Hahn, M. and Kvick, A. (1996a) Microtomography (μ CT) applied to structure analysis of human bone biopsies. *ESRF Newsletter* **25**, 21–23.
- Bonse, U., Busch, F., Beckmann, F. and Günnewig, O. (1996b) Structure variations of human trabecular bone as revealed by SR high resolution microtomography. *J. Synchr. Rad.*, (in preparation).
- Bonse, U., Johnson, Q., Nichols, M., Nußhardt, R., Krasnicki, S. and Kinney, J. (1986) High resolution tomography with chemical specificity. *Nucl. Instrum. Meth. Phys. Res. A* **246**, 644–648.
- Bonse, U., Nußhardt, R., Busch, F., Pahl, R., Johnson, Q., Kinney, J., Saroyan, R. and Nichols, M. (1989) Optimization of CCD based energy modulated X-ray microtomography. *Rev. Sci. Instrum.* **60**, 2478–2481.
- Bonse, U., Nußhardt, R., Busch, F., Pahl, R., Kinney, J., Johnson, Q., Saroyan, R. and Nichols, M. (1991) X-ray tomographic microscopy of fibre-reinforced materials. *J. Mat. Sci.* **26**, 4076–4085.

- Bonse, U., Nußhardt, R., Busch, F., Kinney, J., Saroyan, R. and Nichols, M. (1992) X-ray tomographic microscopy (XTM). In *X-Ray Microscopy III*, pp. 167–176 (eds. A. G. Michette, G. R. Morrison and C. J. Buckley), Springer Verlag, Berlin.
- Borodin, Y. I., Dementyev, E. N., Dragun, G. N., Kulipanov, G. N., Mezentssev, N. A., Pindyurin, V. F., Sheromov, M. A., Skrinsky, A. N., Sokolov, A. S. and Ushakov, V. A. (1986) Scanning X-ray difference microscopy and microtomography using synchrotron radiation of the storage ring VEPP-4. *Nucl. Instrum. Meth. Phys. Res. A246*, 649–654.
- Bowen, D. K. (1989) Microradiography and microtomography. In *Applications of Synchrotron Radiation*, pp. 123–134 (ed. H. Winick), Gordon and Breach.
- Bowen, D. K., Elliott, J. S., Stock, S. R. and Dover, S. D. (1986) X-ray microtomography with synchrotron radiation. *SPIE Proc.—X-Ray Imaging II* **691**, 94–98.
- Boyde, A. (1985) The tandem reflected light microscope, Part II—Pre-Micro '84 applications at UCL. *Proc. R. Microsc. Soc.* **20**, 131–139.
- Boyde, A., Xiao, G., Watson, T., Corle, T. and Kino, G. (1990) An evaluation of unilateral TSM for biological applications. *Scanning* **12**, 273–279.
- Busch, F. (1994) *Auflösungsvermögen einer Mikrotomographie-Kamera für Röntgen-Synchrotronstrahlung*, PhD thesis, Univ. Dortmund, Germany.
- Busch, F., Bonse, U., Beckmann, F., Günnewig, O. and Biermann, T. (1995) A new microtomography camera with increased spatial resolution. *HASYLAB Jahresbericht 1995*, 689–690.
- Castelli, C. M., Allinsons, N. M., Moon, K. J. and Watson, D. L. (1994) High spatial resolution scintillator screens coupled to CCD detectors for X-ray imaging applications. *Nucl. Instrum. Meth. Phys. Res. A348*, 649–653.
- Cazaux, J. (1993) A new quantification procedure for elemental mapping by X-ray (absorption) microscopy. *Microsc. Microanal. Microstruct.* **4**, 513–537.
- Cazaux, J., El Hila, H., Erre, D., Mouze, D., Patat, J.-M., Rondot, S., Trebbia, P. and Zolfaghari, A. (1994) Progress in X-ray projection microscopy. *Microscopy and Analysis*, pp. 19–21.
- Chen, J. W., Xu, Z. Z., Xiao, T. Q., Zhu, P. P., Kou, L. G. and Wang, Z. J. (1995) Aberration analysis and elimination in image reconstruction from X-ray holograms. *Opt. Laser Technol.* **27**, 369–373.
- Chesler, D. A., Riederer, S. J. and Pelc, N. J. (1977) Noise due to photon counting statistics in computed X-ray tomography. *J. Comput. Assist. Tomogr.* **1**, 64–74.
- Davis, G. R. (1994) The effect of linear interpolation of the filtered projections on image noise in X-ray computed tomography. *J. X-Ray Sci. Technol.* **4**, 191–199.
- Deckman, H. W., D'Amico, K. L., Dunsmuir, J. H., Flannery, B. P. and Gruner, S. M. (1989) Microtomography detector design: It's not just resolution. In *Advances in X-Ray Analysis*, pp. 641–650 (eds. C. S. Barrett, J. V. Gilfrich, R. Jenkins, T. C. Huang and P. K. Predecki), Plenum Publishing Corporation.
- Dedrick, D. K., Goulet, R., Huston, L., Goldstein, S. A. and Bole, G. G. (1991) Early bone changes in experimental osteoarthritis using microscopic computed tomography. *J. Rheumatol.* **18**, suppl. **27**, 44–45.
- Delling, G., Hahn, M., Bonse, U., Busch, F., Günnewig, O., Beckmann, F., Uebbing, H. and Graeff, W. (1995) Neue möglichkeiten der strukturanalyse von knochenbiopsien bei anwendung der mikrocomputertomographie (μ CT). *Der Pathologe* **16**, 342–347.
- Dementyev, E. N., Dolbnya, I. P., Kurylo, S. G., Mezentssev, N. A., Pindyurin, V. F. and Sheromov, M. A. (1991) The experimental station for X-ray microscopy and microtomography at the VEPP-3 Storage Ring. *Nucl. Instrum. Meth. Phys. Res. A308*, 352–355.
- Dolbnya, I. P. and Zolotarev, K. V. (1994) X-ray fluorescence microanalysis at the VEPP-3 storage ring in micron spatial resolution region. In *X-Ray Microscopy IV*, pp. 127–135 (eds. V. V. Aristov and A. I. Erko), Bogorodskii Pechatnik Publishing Co., Chernogolovka, Moscow Region.
- Dover, S. D., Elliott, J. C., Boakes, R. and Bowen, D. K. (1988) Three-dimensional X-ray microscopy with accurate registration of tomographic sections. *J. Microsc.* **153**, 187–190.
- Dunsmuir, J. H., Ferguson, S. R., D'Amico, K. L. and Stokes, J. P. (1991) *X-ray microtomography: A new tool for the characterization of porous media*. Proc. 66th Ann. Technic. Conf. of SPE, Oct. 6–9, 1991, pp. 423–430.
- Dunsmuir, J. H., Ferguson, S. R. and D'Amico, K. L. (1992) *Design and operation of an X-ray detector for microradiography*. Proc. Conf. on Photoelectronic Image Devices, London, September 1991, pp. 257–264.
- Elliott, J. C., Anderson, P., Davis, G. R., Dover, S. D., Stock, S. R., Breunig, T. M., Guvenilir, A. and Antolovich, S. D. (1990) Application of X-ray microtomography in materials science illustrated by a study of a continuous fiber metal matrix composite. *J. X-Ray Sci. Technol.* **2**, 249–258.
- Elliott, J. C., Anderson, P., Gao, X. J., Wong, F. S. L., Davis, G. R. and Dowker, S. E. P. (1994a) Application of scanning microradiography and X-ray microtomography to studies of bones and teeth. *J. X-Ray Sci. Technol.* **4**, 102–117.
- Elliott, J. C., Anderson, P., Davis, G. R., Wong, F. S. L. and Dover, S. D. (1994b) Computed tomography part II: The practical use of a single source and detector. *J. Metals* **46**, 11–19.
- Elliott, J. C., Boakes, R., Dover, S. D. and Bowen, D. K. (1987a) Biological applications of microtomography. In *X-ray Microscopy II*, pp. 349–355 (eds. D. Sayre, M. Howells, J. Kirz and H. Rarback), Springer-Verlag, Berlin.
- Elliott, J. C., Bowen, D. K., Dover, S. D. and Davies, S. T. (1987b) X-ray microtomography of biological tissues using laboratory and synchrotron sources. *Biol. Trace Elem. Res.* **13**, 219–227.
- Engelke, K., Graeff, W., Meiss, L., Hahn, M. and Delling, G. (1993) High spatial resolution of bone mineral using computed microtomography—comparison with microradiography and undecalcified histologic sections. *Invest. Radiol.* **28**, 341–349.
- Engelke, K., Lohmann, M., Dix, W.-R. and Graeff, W. (1989a) Quantitative microtomography. *Rev. Sci. Instrum.* **60**, 2486.
- Engelke, K., Lohmann, M., Dix, W.-R. and Graeff, W. (1989b) A system for dual energy microradiography of bones. *Nucl. Instrum. Meth. Phys. Res. A274*, 380–389.

- Feldkamp, L. A., Davis, L. C. and Kress, J. W. (1984) Practical cone-beam algorithm. *J. Opt. Soc. Am.* **A1**, 612–619.
- Feldkamp, L. A., Goldstein, S. A., Parfitt, A. M., Jesion, G. and Kleerekoper, M. (1989) The direct examination of three-dimensional bone architecture *in vitro* by computed tomography. *J. Bone Miner. Res.* **4**, 3–11.
- Fischer, B. E. and Mühlbauer, C. (1990) Microtomography by heavy ions. *Nucl. Instrum. Meth. Phys. Res.* **B47**, 271–282.
- Flannery, B. P., Deckman, H. W., Roberge, W. G. and D'Amico, K. L. (1987) Three-dimensional X-ray microtomography. *Science* **237**, 1439–1444.
- Fuhrmann, G. (1993) *Entwicklung eines Mikrotomographiesystems als Zusatz für Rasterelektronenmikroskope*. PhD thesis, Forschungszentrum Jülich, Germany.
- Gao, X. J., Elliott, J. C., Anderson, P. and Davis, G. R. (1993) Scanning microradiographic and microtomographic studies of remineralization of subsurface enamel lesions. *J. Chem. Soc. Faraday Trans.* **89**, 2907–2912.
- Goldstein, S. A., Goulet, R. and McCubrey, D. (1993) Measurement and significance of three-dimensional architecture to the mechanical integrity of trabecular bone. *Calcif. Tissue Int.* **53**, suppl. 1, S127–S133.
- Goulet, R. W., Goldstein, S. A., Ciarelli, M. J., Kuhn, J. L., Brown, M. B. and Feldkamp, L. A. (1994) The relationship between the structural and orthogonal compressive properties of trabecular bone. *J. Biomech.* **27**, 375–389.
- Graeff, W. and Engelke, K. (1991) Microradiography and microtomography. In *Handbook on Synchrotron Radiation*, pp. 361–405 (eds. S. Ebashi, M. Koch and E. Rubinstein), Elsevier Science.
- Graeff, W. (1996) Biomedical application of microtomography. In *Proceedings of the International School of Physics "Enrico Fermi", Course CXXVII: "Biomedical Applications of Synchrotron Radiation"*, pp. 155–170 (eds. E. Burattini and A. Balerna), IOS Press, Amsterdam.
- Grodzins, L. (1983) Optimum energies for X-ray transmission tomography of small samples. *Nucl. Instrum. Meth. Phys. Res.* **206**, 541–545.
- Günnewig, O. (1996) *3D-Mikrotomographische Strukturuntersuchung und -darstellung von Knochenbiopsien mit konventionellen Röntgenquellen und Synchrotronstrahlung*. PhD thesis, Univ. Dortmund, Germany.
- Gurker, N., Nell, R., Backfrieder, W., Kandutsch, J., Sarg, K., Prevrhal, S. and Nentwich, C. (1994) X-ray microtomography experiments using a diffraction tube and a focusing multilayer-mirror. *Nucl. Instrum. Meth. Phys. Res.* **B94**, 154–171.
- Haddad, W. S., McNulty, I., Trebes, J. E., Anderson, E. H., Levesque, R. A. and Yang, L. (1994) Ultrahigh-resolution X-ray tomography. *Science* **266**, 1213–1215.
- Hirano, T. and Usami, K. (1989) High resolution monochromatic X-ray tomography using synchrotron radiation. *Jpn. J. Appl. Phys.* **28**, 263–266.
- Hirano, T., Eguchi, S. and Usami, K. (1989a) Study of quantitative elemental analysis of monochromatic X-ray CT using synchrotron radiation. *Jpn. J. Appl. Phys.* **28**, 135–139.
- Hirano, T., Funaki, M., Nagata, T., Taguchi, I., Hamada, H., Usami, K. and Hayakawa, K. (1990) Observation of allende and antarctic meteorites by monochromatic X-ray CT based on synchrotron radiation. In *Proceedings of the NIPR Symposium on Arctic Meteorites*, No. 3, pp. 270–281 (ed. National Institute of Polar Research, Tokyo).
- Hirano, T., Usami, K. and Sakamoti, K. (1989b) High resolution monochromatic tomography with X-ray sensing pickup tube. *Rev. Sci. Instrum.* **60**, 2482–2485.
- Hirano, T., Usami, K., Tanaka, Y. and Masuda, C. (1995) *In situ* X-ray CT under tensile loading using synchrotron radiation. *J. Mater. Sci.* **10**, 381–386.
- Hounsfield, G. (1973) Computerized transverse axial scanning (tomography), Part 1. *Br. J. Radiol.* **46**, 1016–1051.
- Huddleston, J., Hutchinson, I. G., Pierce, T. B. and Foster, J. (1982) Development and comparison of techniques for two-dimensional analysis using the Harwell nuclear microprobe. *Nucl. Instrum. Meth. Phys. Res.* **197**, 157–164.
- Ito, A. and Koyama-Ito, H. (1984) Possible use of proton CT as means of density normalization in the PIXE semi-microprobe analysis. *Nucl. Instrum. Meth. Phys. Res.* **B3**, 584–588.
- Johnson, Q., Kinney, J., Bonse, U., Nichols, M., Nußhardt, R. and Brase, J. (1986) Microtomography using synchrotron radiation. *Mat. Res. Soc. Symp. Proc.* **69**, 203–208.
- Jones, R. (1959) Quantum efficiency of detectors for visible and infrared radiation. *Adv. Electron. Electron Phys.* **11**, 87–183.
- Jönsson, E. (1928) *Absorptionsmessungen im langwelligen Röntgengebiet und Gesetz der Absorption*. PhD thesis, Uppsala.
- Kak, A. C. and Slaney, M. (1987) *Principles of Computerized Tomographic Imaging*. IEEE Press, New York.
- King, W. E., Campbell, G. H., Haupt, D. L., Kinney, J. H., Riddle, R. A. and Wien, W. L. (1995) X-ray tomographic microscopy investigation of the ductile rupture of an aluminium foil bonded between sapphire blocks. *Scr. Metall.* **33**, 1941–1946.
- Kinney, J. H. and Nichols, M. C. (1992) X-ray tomographic microscopy (XTM) using synchrotron radiation. *A. Rev. Mater. Sci.* **22**, 121–152.
- Kinney, J. H., Balooch, M., Marshall, S. J. and Marshall, G. W. (1995a) Mineral distribution and dimensional changes in human dentin during demineralization. *J. Dent. Res.* **74**, 1179–1184.
- Kinney, J. H., Balooch, M., Marshall, S. J., Marshall, G. W. and Weihs, T. M. (1996a) Hardness and Young's modulus of peritubular and intertubular dentin. *Arch. Oral Biol.* **41**, 9–13.
- Kinney, J. H., Balooch, M., Marshall, G. W., Marshall, S. J. and Weihs, T. M. (1996b) Atomic force microscope measurement of the hardness and elasticity of peritubular and intertubular human dentin. *J. Biomech. Eng.* **118**, 133–135.
- Kinney, J. H., Breunig, T. M., Starr, T. L., Haupt, D., Nichols, M. C., Stock, S. R., Butts, M. D. and Saroyan, R. A. (1993) X-ray tomographic study of chemical vapor infiltration processing of ceramic composites. *Science* **260**, 789–792.

- Kinney, J. H., Haupt, D. L., Nichols, M. C., Breunig, T. M., Marshall, G. W. and Marshall, S. J. (1994a) The X-ray tomographic microscope: Three-dimensional perspectives of evolving microstructures. *Nucl. Instrum. Meth. Phys. Res. A* **347**, 480–486.
- Kinney, J. H., Haupt, D. L., White, J. M., Bell, W. L., Balooch, M., Marshall, S. J. and Marshall, G. W. Jr. (1996c) The effects of Nd and Ho:YAG laser-induced surface modification on demineralization of dentin surfaces. *J. Dent. Res.*, (to be published).
- Kinney, J. H., Henry, C. P., Haupt, D. L. and Starr, T. L. (1994b) The topology of percolating porosity in woven fiber ceramic matrix composites. *Appl. Compos. Mater.* **1**, 325–331.
- Kinney, J., Johnson, Q., Nichols, M., Bonse, U. and Nußhardt, R. (1986a) Elemental and chemical-state imaging using synchrotron radiation. *Appl. Opt.* **25**, 4583–4585.
- Kinney, J., Johnson, Q., Bonse, U., Nußhardt, R. and Nichols, M. (1986b) The performance of CCD array detectors for application in high-resolution tomography. *SPIE Proc.—X-Ray Imaging II* **691**, 43–50.
- Kinney, J., Johnson, Q., Bonse, U., Nichols, M., Saroyan, R., Nußhardt, R., Pahl, R. and Brase, J. (1988) Three-dimensional X-ray computed tomography in materials science. *MRS Bull.* **XIII**, 13–17.
- Kinney, J. H., Lane, N. E. and Haupt, D. L. (1995b) *In vivo*, 3-D morphometry of trabecular bone. *J. Bone Miner. Res.* **10**, 264–272.
- Kinney, J. H., Nichols, M. C., Bonse, U., Stock, S. R., Breunig, T. M., Guvenilir, A. and Saroyan, R. A. (1991a) Nondestructive imaging of materials microstructures using X-ray tomographic microscopy. *Mat. Res. Soc. Symp. Proc.* **217**, 81–95.
- Kinney, J. H., Saroyan, R. A., Massey, W. A., Nichols, M. C., Bonse, U. and Nußhardt, R. (1991b) X-ray tomographic microscopy for nondestructive characterization of composites. *Rev. Prog. Quant. Nondest. Eval.* **10A**, 427–433.
- Kinney, J., Stock, S., Nichols, M., Bonse, U., Breunig, T., Saroyan, R., Johnson, Q., Nußhardt, R., Busch, F. and Antolovich, S. (1989) Nondestructive investigation of damage in composites using X-ray tomographic microscopy (XTM). *J. Mater. Res.* **5**, 1123–1129.
- Knor, I. B., Naumova, E. N., Trounova, V. A., Dolbnya, I. P. and Zolotarev, K. V. (1995) Biological monitoring of meadow moths by SR-XRF technique. *Nucl. Instrum. Meth. Phys. Res. A*, (in press).
- Kuhn, J. L., Goldstein, S. A., Feldkamp, L. A., Goulet, R. W. and Jesion, G. (1990) Evaluation of a microcomputed tomography system to study trabecular bone structure. *J. Orthopaed. Res.* **8**, 833–842.
- Lane, N. E., Strewler, G. J., Thompson, J. M. and Kinney, J. H. (1995) Intermittent treatment with human parathyroid hormone (hPTH 1-34) increased trabecular bone volume but not connectivity in osteopenic rats. *J. Bone Miner. Res.* **10**, 1179–1184.
- Layton, M. W., Goldstein, S. A., Goulet, R. W., Feldkamp, L. A., Kubinski, D. J. and Bole, G. G. (1988) Examination of subchondral bone architecture in experimental osteoarthritis by microscopic computed axial tomography. *Arthritis and Rheumatism* **31**, 1400–1405.
- Lehr, J. (1996) 3D X-ray microscopy: Tomographic imaging of mineral sheaths of bacteria *Leptothrix ochracea* with the Göttingen X-ray microscope at BESSY, Optik (in press).
- Majumdar, S., Newitt, D., Mathur, A., Osman, D., Gies, A., Chiu, E., Lotz, J., Kinney, J. H. and Genant, H. (1996) Magnetic resonance (MR) imaging of trabecular bone structure in the distal radius: Comparison with X-ray tomographic microscopy and biomechanics. *Osteoporosis Int.* (in press).
- Mandel, L. (1959) Image fluctuations in cascade intensifiers. *Br. J. Appl. Phys.* **10**, 233–234.
- Masuda, C., Tanaka, Y., Hirano, K., Usamy, T., Imai, Y., Shiota, I., Furubayashi, E. and Iwasaki, H. (1992) Observation of fibers in long fiber reinforced metal matrix composites by X-ray computed tomography using synchrotron radiation. *Nondest. Test. Eval.* **8–9**, 779–786.
- McNulty, I. (1994) The future of X-ray holography. *Nucl. Instrum. Meth. Phys. Res. A* **347**, 170–176.
- McNulty, I., Haddad, W. S., Trebes, J. E. and Anderson, E. H. (1995) Soft X-ray scanning microtomography with submicrometer resolution. *Rev. Sci. Instrum.* **66**, 1431–1433.
- McNulty, I., Kirz, J., Jacobsen, C., Anderson, E. H., Howells, M. R. and Kern, D. P. (1992a) High-resolution imaging by Fourier transform X-ray holography. *Science* **256**, 1009–1012.
- McNulty, I., Trebes, J. E., Brase, J. M., Yorkey, T. J., Levesque, R., Szoke, H., Andersen, E. H., Jacobsen, C. and Kern, D. (1992b) Experimental demonstration of high resolution three-dimensional X-ray holography. *SPIE Proc.—Soft X-Ray Microscopy* **1741**, 78–84.
- Meyer-Ilse, W., Guttmann, P., Thieme, J., Rudolph, D., Schmahl, G., Anderson, E., Batson, P., Attwood, D., Iskander, N. and Kern, D. (1992) Experimental characterization of zone plates for high resolution X-ray microscopy. In *X-ray Microscopy III*, pp. 284–289 (eds. A. G. Michette, G. R. Morrison, and C. J. Buckley), Springer-Verlag, Berlin.
- Mezentsev, N. A. and Pindiurin, V. F. (1987) Application of synchrotron radiation to medical diagnostics at Novosibirsk: Status and prospects. *Nucl. Instrum. Meth. Phys. Res. A* **261**, 301–307.
- Momose, A. and Fukuda, J. (1995) Phase-contrast radiographs of non-stained rat cerebellar specimen. *Med. Phys.* **22**, 375–379.
- Momose, A. (1995) Demonstration of phase-contrast X-ray computed tomography using an X-ray interferometer. *Nucl. Instrum. Meth. Phys. Res. A* **352**, 622–628.
- Momose, A., Takeda, T. and Itai, Y. (1995) Phase-contrast X-ray computed tomography for observing biological specimens and organic materials. *Rev. Sci. Instrum.* **66**, 1434–1436.
- Momose, A., Takeda, T., Itai, Y. and Hirano, K. (1996) Phase-contrast X-ray computed tomography for observing biological soft tissues. *Nature Medicine* **2**, 473–475.
- Mummery, P. M., Anderson, P., Davis, G. R., Derby, B. and Elliott, J. C. (1993) Damage assessment in particle-reinforced metal matrix composites using X-ray microtomography. *Scripta Metallurgica et Materialia* **29**, 1457–1462.
- Nagata, Y., Yamaji, H., Hayashi, K., Kawashima, K., Hyodo, K., Kawata, H. and Ando, M. (1992) High energy, high resolution monochromatic X-ray computed tomography system. *Res. Nondest. Eval.* **4**, 55–78.
- Nichols, M. C., Kinney, J. H., Johnson, Q. C., Saroyan, R. A., Bonse, U., Nußhardt, R. and Pahl, R. (1989) Synchrotron microtomography of supported catalysts. *Rev. Sci. Instrum.* **60**, 2475–2477.

- Nußhardt, R. (1990) *Elementspezifische und hoch ortsauflösende Mikrotomographie mit Synchrotronstrahlung*, PhD thesis, Univ. Dortmund, Germany.
- Nußhardt, R., Bonse, U., Busch, F., Kinney, J., Saroyan, R. and Nichols, M. (1991) Microtomography: A tool for nondestructive study of materials. *Synchr. Rad. News* 4, 21–23.
- Parfitt, A. M., Drezner, M. K., Glorieux, F. H., Kanis, J. A., Malluche, H., Meunier, P. J., Ott, S. M. and Recker, R. R. (1987) Bone histomorphometry: Standardization of nomenclature, symbols, and units. *J. Bone Min. Res.* 2, 595–610.
- Petran, M., Hadravsky, M., Benes, J., Kucera, P. and Boyde, A. (1985) The tandem reflected light microscope, Part I—The principle and its design. *Proc. R. Microsc. Soc.* 20, 125–129.
- Pontau, A. E., Antolak, A. J., Morse, D. H., Ver Berkmoos, A. A., Brase, J. M., Heikkinen, D. W., Martz, H. E. and Proctor, I. D. (1989) Ion microbeam tomography. *Nucl. Instrum. Meth. Phys. Res.* B40, 646–650.
- Pontau, E., Antolak, A. and Morse, D. (1990) Some practical considerations for ion microtomography. *Nucl. Instrum. Meth. Phys. Res.* B45, 503–507.
- Radon, J. (1917) Über die Bestimmung von Funktionen durch ihre Integralwerte längs gewisser Mannigfaltigen, *Ber. Verh. Sächs. Akad. Wiss. Leipzig, Math. Phys. Kl.* 69, 262–277.
- Rüeggsegger, P., Koller, B. and Müller, R. (1996) A microtomographic system for the nondestructive evaluation of bone architecture. *Calcif. Tissue Int.* 58, 24–29.
- Sasov, A. Y. and Cazaux, J. (1994) Investigation of electronic components by X-ray microscopy and microtomography. In *X-Ray Microscopy IV*, pp. 157–163 (eds. V. V. Aristov and A. I. Erko), Bogorodskii Pechatnik Publishing Co., Chernogolovka, Moscow Region.
- Schlenker, M., Bauspiess, W., Graeff, W., Bonse, U. and Rauch, H. (1980) Imaging of ferromagnetic domains by neutron interferometry. *J. Magn. Mater.* 15–18, 1507–1509.
- Schütz, G., Wagner, W., Wilhelm, W., Kienle, P., Zeller, R., Frahm, R. and Materlik, G. (1987) Absorption of circularly polarized X-rays in iron. *Phys. Rev. Lett.* 58, 737–740.
- Snigirev, A., Snigireva, I., Kohn, V., Kuznetsov, S. and Schekolov, I. (1995) On the possibilities of X-ray phase contrast microimaging by coherent high-energy synchrotron radiation. *Rev. Sci. Instrum.* 66, 5486–5492.
- Stock, S., Kinney, J., Breunig, T., Bonse, U., Antolovich, S., Johnson, Q. and Nichols, M. (1989) Synchrotron microtomography of composites. *Mat. Res. Symp. Proc.* 143, 273–278.
- Suzuki, Y., Hayakawa, K., Usami, K., Hirano, T., Endoh, T. and Okamura, Y. (1989) X-ray sensing pickup tube. *Rev. Sci. Instrum.* 60, 2299–2302.
- Suzuki, Y., Hirano, T. and Usami, K. (1990) X-ray microtomography using synchrotron radiation. In *X-Ray Microscopy in Biology and Medicine*, pp. 179–190 (eds. K. Shinohara *et al.*), Japan Sci. Soc. Press, Tokyo / Springer-Verlag, Berlin.
- Suzuki, Y., Usami, K., Sakamoto, K., Kozaka, H., Hirano, T., Shinono, H. and Kohno, H. (1988) X-ray computerized tomography using synchrotron radiation. *Jpn. J. Appl. Phys.* 27, L461–L464.
- Takeda, T., Itai, Y., Hayashi, K., Nagata, Y., Yamaji, H. and Hyodo, K. (1994) High spatial resolution CT with a synchrotron radiation system. *J. Comput. Assist. Tomogr.* 18, 98–101.
- Tanak, Y., Masuda, C., Hirano, T., Usami, K. and Hishijima, S. (1993) *In situ* observation of MMC under tensile loading by synchrotron X-ray CT. *Proc. Jap. Int. SAMPE Symp.* 2, 2141–2146.
- Thomas, X., Cazaux, J., Erre, D., Mouze, D. and Collard, P. (1992) X-ray projection microscopy and microtomography in a scanning electron microscope. In *X-Ray Microscopy III*, pp. 190–194 (eds. A. G. Michette, G. R. Morrison, and C. J. Buckley), Springer-Verlag, Berlin.
- Zhou, X. and Lauterbur, P. C. (1992) NMR microscopy using projection reconstruction. In *Magnetic Resonance Microscopy. Methods and Application in Materials Science, Agriculture and Biomedicine*, pp. 3–27 (eds. B. Blümich and W. Kuhn), VCH Verlagsgesellschaft, Weinheim.
- Zywicz, E., Kinney, J. H., Sattler, M. L., Breunig, T. M. and Nichols, M. C. (1993) Heterogeneous fibre microstructures and their influence on failure. *J. Microsc.* 169, 247–253.